Faculty of Sciences

Academic year 2013–2014

Investigation of muon background in the prototype antineutrino detector for the SoLid experiment

Céline Moortgat

Promotor: Prof. Dr. D. Ryckbosch

Submitted in partial fulfillment of the requirements for the degree of Master in Physics and Astronomy

Acknowledgements

First of all, I would like to thank Prof. Dr. Dirk Ryckbosch for giving me the opportunity to be a part of the SoLid collaboration. I've had so much fun working on this project and I have enjoyed being able to work in this dynamic group, which would not have been possible without him. I am also grateful to all the other members of the group for tolerating me in their weekly video conferences and helping me with different aspects of my thesis.
Thanks to Nick Ryder and Petra Van Mulders for helping me with the analysis of the muon signals and for providing a lot of useful comments on my plots and results during meetings. To Prof. Dr. Nick van Remortel, Dr. Paul Scovell and Sara Alderweireldt for helping me get started with the NEMENIX simulation. I also wish to thank Philippe Van Auwegem for all the help regarding technical issues.
I'm very grateful to Sander Vanheule, who voluntarily, almost at least, helped me with practical issues, bugs in my code and proofreading of this thesis. For the latter, I also wish to thank Matthias Vraeghe. Thank you to Mathieu Labare for discussing the error calculations with me.
Without all my friends at the INW campus this would not have been such a great experience. So thanks to my fellow thesis students for all the chats, lunches and discussions.

Céline Moortgat
Ghent, June 2014

Contents

List of Figures

List of Tables

Introduction

Neutrinos belong to the most fascinating particles discovered so far. This is due to the fact that neutrinos are so difficult to capture as they only interact via the weak interaction. They are described in the Standard Model but experiments have shown that not all properties of neutrinos fit into this particle physics framework. They have, for example, a non-zero mass which allows them to oscillate into different neutrino flavors. A lot of experiments have been performed to investigate the oscillation parameters and a fairly consistent picture of 3 neutrino flavors oscillating into each other was formed.

Since the mid 90s however, experiments started to point towards an inconsistency in the oscillation picture which will be discussed in chapter 1. Results from accelerator, radioactive source and reactor experiments all show effects that could be explained by new physics. More precisely, by the existence of a sterile, not weakly interacting, neutrino. To provide a conclusive explanation for the neutrino anomaly, a short-baseline reactor or a radioactive source experiment with a good spatial and energy resolution needs to be built.

The SoLid experiment, which will be discussed in chapter 2, is one such short-baseline experiment, located at the BR2 reactor at the SCK•CEN at Mol in Belgium. The principle of the detector relies on an inverse beta decay interaction with a proton of the detector material. So far, a prototype of the detector has been built and is currently, May 2014, still taking data at the BR2 reactor. The prototype is called NEMENIX and its construction and data-taking stage should provide very useful information for the SoLid detector.

As NEMENIX is a lot smaller than the dimensions planned for SoLid, more care has to be taken to eliminate backgrounds. To be able to identify muons in NEMENIX more easily, extra muon detectors were installed at the BR2 reactor. They were built in Ghent and their efficiencies were measured in the context of this thesis. A C++ simulation was written to estimate the influence of geometrical effects of the setup on the measured efficiencies. The operating parameters were also determined, such as the thresholds and HV power settings. These aspects will be discussed in chapter 3.

After the installation of the muon detectors at the reactor site, the properties of muon signals could be investigated. In chapter 4 the analysis of single signals and muon coincidences will be treated, as well as the rate of muons and geometrical effects at BR2.

In chapter 5 the conclusions of the previous 2 chapters will be summarized and an outlook will be given concerning further steps in the muon background identification in NEMENIX and SoLid.

Chapter 1

Neutrino physics

1.1 The Standard Model

The Standard Model (SM) describes all known subatomic particles, this particle physics theory also explains the forces through which these particles interact. These include the electromagnetic, the strong and the weak force. The fourth fundamental force, gravity, is not included in the SM as it has, up to now, not been possible to incorporate quantum physics and general relativity in the same framework. Although gravity is a very important force on large scales, it can luckily be neglected on the scale of subatomic physics.

The 12 elementary particles that constitute all matter can be divided into two groups of 6 particles, the quarks and the leptons [1], shown in table 1.1. All of them are fermions, which means they have a half-integer spin. Every elementary particle has an antiparticle which has the same mass but opposite quantum numbers such as those shown in table 1.1. For each charged lepton, a corresponding neutrino exists. They are arranged in a doublet structure which means that they have opposite values for the weak isospin. Both quarks and leptons consist out of 3 families or generations. The second and third generation can be regarded a heavier version of the first family. Ordinary matter which we can find around us is made up of particles from the first family, such as up and down quarks and electrons. Particles that are composed out of quarks are called hadrons and together represent the hadron zoo. Particles that consist out of 3 quarks are called baryons, the neutron, uud (2 up quarks and 1 down quark), and proton, udd (1 up quark and 2 down quarks), belong to this category. Pions and kaons are two examples of hadrons which each contain 2 quarks, the so called mesons. Apart from the fermions, the SM also incorporates integer spin particles. These are the bosons that mediate the forces between the particles.

In table 1.1 all the elementary fermions, their generation number and important properties are listed. The color and weak isospin are properties of the particles which are related to respectively the strong and the weak interaction. The leptons do not have color and therefore do not interact via the strong force. The charge of the particles determines

whether they interact electromagnetically. The three particle properties mentioned above are conserved quantities in all fundamental interactions.

Table 1.1: The elementary fermions [2].

Fermions	Generation	Name	Symbol	Mass (MeV/c^2)	Charge (e)	Weak isospin	Color
Quarks	I	up	u	2.3	+2/3	+1/2	r, g, b
		down	d	4.8	-1/3	-1/2	r, g, b
	II	charm	c	1.28×10^3	+2/3	+1/2	r, g, b
		strange	s	95	-1/3	-1/2	r, g, b
	III	top	t	173.5×10^3	+2/3	+1/2	r, g, b
		bottom	b	4.7×10^3	-1/3	-1/2	r, g, b
Leptons	I	electron	e	0.511	-1	-1/2	–
		electron neutrino	ν_e	$< 2.2 \times 10^{-6}$	0	+1/2	–
	II	muon	μ	105.7	-1	-1/2	–
		muon neutrino	ν_μ	< 0.19	0	+1/2	–
	III	tau	τ	1777	-1	-1/2	–
		tau neutrino	ν_τ	< 18.2	0	+1/2	–

1.2 History of neutrinos

One of the most mysterious particles known to man is the neutrino. Its existence was first proposed by Pauli in 1930, who wanted to explain the experimental results concerning beta decay. Without the neutrino, beta decay would be the process of converting a neutron to a proton with creation of an electron:

$$n \rightarrow p + e^- \tag{1.1}$$

This would result in a fixed kinetic energy of the beta particle (electron), approximately equal to the energy released in the process $Q = M_{(A,Z)} - M_{(A,Z+1)} - m_e$. This was not in agreement with the continuous beta spectrum, with an end energy of Q_β, recorded in experiments shown in figure 1.1. This energy loss could only be explained by the creation of a neutral, and thus undetected, particle that caries away some fraction of the energy. Beta decay therefore can be represented by:

$$n \rightarrow p + e^- + \bar{\nu}_e \tag{1.2}$$

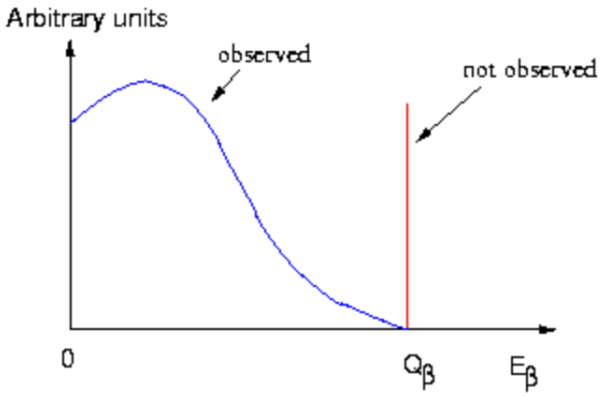

Figure 1.1: The kinetic energy spectrum of the emitted electron in β-decay process (observed). If no antineutrino could be emitted, the total available energy should be carried by the electron and we should observe a peak at E_β=Q_β (not observed) [3].

Building on the idea of Pauli, Enrico Fermi developed his theory of beta decay. He gave the particle the name "neutrino", which means "little neutral one" in Italian. He also assumed the particle to be massless [4].

In 1956 F. Reines and C. Cowan conducted the first experiment able to detect neutrinos. For this they received the Nobel Prize in Physics in 1995. By doing their experiment they disproved Pauli, who said that neutrinos would never be detected. Because of the very weakly interacting nature of neutrinos, one needed a source with a larger neutrino flux than that of radioactive sources to be able to capture the elusive particles. This became possible with the installation of nuclear reactors, which had an expected flux of 10^{12} to

10^{13} neutrinos per second per cm^2. Cowan and Reines conducted their research at the Hanford reactor and the Savannah River Plant. The detection of neutrinos required the interaction with a proton from the target water tank. This would then create a neutron and a positron:

$$\bar{\nu}_e + p \rightarrow n + e^+ \tag{1.3}$$

Both of these particles needed to be detected to obtain a statistically significant signal. High background and low counting rate caused a lot of problems, but eventually they were able to state the existence of a free antineutrino [5].

The next episode in the history of the neutrino was the discovery of the muon neutrino. Up to 1962 only the electron neutrino was known but with the construction of the Alternating Gradient Synchrotron (AGS) the creation of a proton beam with high enough energy to conduct the experiment became possible. This beam could then create a beam of pions (π) when directed on a beryllium target. These would then decay into muons and muon neutrinos:

$$\pi \rightarrow \mu + \nu_\mu \tag{1.4}$$

The neutrinos were then detected in a spark chamber. For the discovery of the muon neutrino and thus demonstrating the doublet structure of leptons Leon Lederman, Melvin Schwartz and Jack Steinberger received the Nobel Prize in Physics in 1988 [6].

After the discovery of the charm quark in 1974 the structure of 2 families became even more pronounced. As nobody knew why there would only be 2 generations, some questioned why there could not be more. This idea gained more support after M. Perl published evidence of events that could indicate the decay of a new heavy lepton [7]. This lepton was represented by the symbol τ, derived from the greek word $\tau\rho\iota\tau o\upsilon$ (triton), which means "third". The corresponding neutrino, ν_τ, was discovered in 2000 by the DONUT Collaboration [8]. Following the generation structure, heavier quarks were expected to complete the third family. These were the bottom and the top quark discovered respectively in 1977 [9] and 1995 [10] at FNAL. In 1989 it was confirmed that there are three, and no more than 3, types of light, weakly-interacting neutrinos. This was observed through the lifetime of the Z boson [11]. The more particles the Z boson can decay to, the shorter the lifetime and the larger the width of the mass distribution. In figure 1.2 one can see that the data match the curve corresponding to 3 light neutrino flavors ($N_\nu = 3$).

Another chapter in the understanding of the neutrino was the verification that the sun is powered by nuclear fusion reactions:

$$4p \rightarrow {}^4He + 2e^+ + 2\nu_e \tag{1.5}$$

Raymond Davis Jr. and John N. Bahcall proposed to prove this theory by detecting solar neutrinos with the help of a very large tank of cleaning fluid. When the first results of

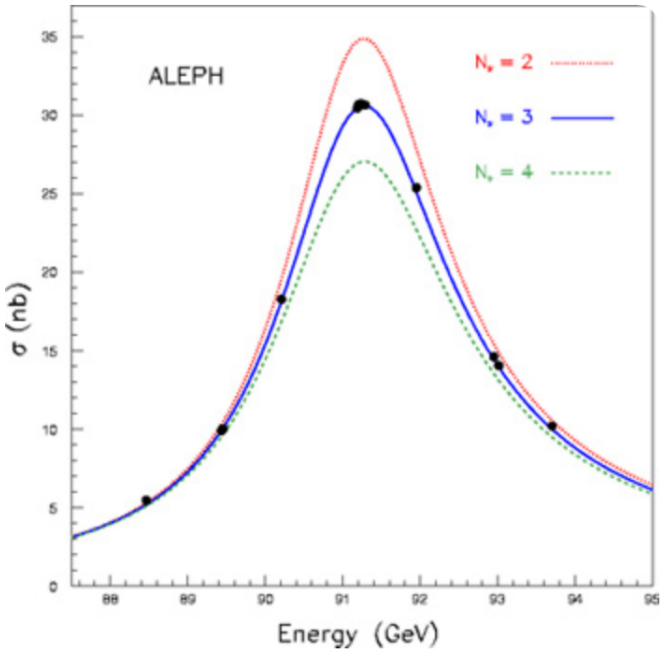

Figure 1.2: Points indicating the measured mass distribution of the Z boson. The lines are predictions corresponding to the different N_ν hypotheses [12].

the Homestake Experiment were published in 1968 there seemed to be a sizable difference between the measured and predicted amount of neutrinos [13]. There were a lot of different explanations for this discrepancy. There could have been a problem with the understanding of the sun, the experiment might have been faulty, the prediction of the rate of captured neutrinos could be wrong or maybe something else happened to the neutrinos escaping the sun. In 1989 the Kamiokande group published results similar to the defect Davis had encountered [14]. This pointed into the direction of a real physical effect in contrast to a mistake in the experiment itself as an explanation for the solar neutrino problem.

Aside from the solar neutrinos, atmospheric neutrinos did not behave according to theory either. One expects to have a 2:1 ratio of muon to electron neutrinos from cosmic rays. This is due to the creation of hadrons, mostly pions, when the primary cosmic rays hit the atmosphere. These pions decay into a muon and a muon neutrino. In turn, the muon decays to an electron, an electron neutrino and another muon neutrino.

$$\pi \rightarrow \mu + \nu_\mu \tag{1.6}$$

$$\mu \rightarrow e + \nu_e + \nu_\mu \tag{1.7}$$

This ratio was not in agreement with the experimental results from different collaborations. Kamiokande obtained a ratio of 0.60 ± 0.08 and the IMB-3 (the Irvine-Michigan-Brookhaven detector) 0.54 ± 0.13 [15].

1.3 Neutrino oscillations

The combined result of the solar and atmospheric neutrino anomalies, discussed in section 1.2, gives a strong indication for new physics. Up to the nineties it was believed that lepton family number was conserved, which means that an electron neutrino cannot change into a different type or flavor of neutrino. But with the growing amount of experimental data the idea of neutrino oscillations, proposed by Bruno Pontecorvo in 1957 [16], gained support. This would also imply that the neutrino can not be massless and that all the flavors also have a different mass. Neutrino oscillations could explain the low amount of muon neutrinos from atmospheric events as these would change into a different type of neutrino before reaching the detector. Similarly, electron neutrinos coming from the sun would be able to change into a different flavor, thereby explaining the deficit observed in experiments.

The phenomena of neutrino oscillations is due to the fact that neutrino flavors are each a superposition of 3 mass eigenstates. When neutrinos are created in a weak process, they have a definite flavor but when they travel a certain distance this changes. This occurs because the quantum mechanical phases of the different mass states progress at a different rate. Therefore there is a change in superposition of mass states, this implies also a different mixture of flavor eigenstates. As the advancing of the quantum mechanical phases is periodical a neutrino will eventually end up in its original flavor. The mass and flavor eigenstates can be related by a unitary transformation [17]:

$$|\nu_i\rangle = \Sigma_\alpha U^*_{\alpha i}|\nu_\alpha\rangle \tag{1.8}$$

$$|\nu_\alpha\rangle = \Sigma_i U_{\alpha i}|\nu_i\rangle \tag{1.9}$$

where $|\nu_i\rangle$ is a neutrino with a definite mass (i = 1, 2, 3), $|\nu_\alpha\rangle$ is a neutrino of a definite flavor (α = e, μ, τ) and $U_{\alpha i}$ represents the Pontecorvo-Maki-Nakagawa-Sakata matrix.

$$\begin{aligned} U_{\alpha i} &= \begin{pmatrix} U_{e1} & U_{e2} & U_{e3} \\ U_{\mu 1} & U_{\mu 2} & U_{\mu 3} \\ U_{\tau 1} & U_{\tau 2} & U_{\tau 3} \end{pmatrix} \\ &= \begin{pmatrix} c_{12}c_{13} & s_{12}c_{13} & s_{13}e^{-i\delta} \\ -s_{12}c_{23} - c_{12}s_{23}s_{13}e^{i\delta} & c_{12}c_{23} - s_{12}s_{23}s_{13}e^{i\delta} & s_{23}c_{13} \\ s_{12}s_{23} - c_{12}c_{23}s_{13}e^{i\delta} & -c_{12}s_{23} - s_{12}c_{23}s_{13}e^{i\delta} & c_{23}c_{13} \end{pmatrix} \times \begin{pmatrix} 1 & 0 & 0 \\ 0 & e^{i\alpha_1/2} & 0 \\ 0 & 0 & e^{i\alpha_2/2} \end{pmatrix} \end{aligned} \tag{1.10}$$

where $c_{ij} = \cos\theta_{ij}$, $s_{ij} = \sin\theta_{ij}$ and θ is the mixing angle. The values of the parameters α_1, α_2 and δ are still to be determined, if they are non-zero at all. The alpha phase factors are only appropriate when the neutrino would be identical to its antineutrino, which means they would be Majorana particles. The delta parameter is expected to have a non-zero

value if neutrino oscillations violate CP symmetry [1].

Calculations [17] show that the probability that a neutrino of flavor α, with an energy E, becomes a neutrino of flavor β after traveling a distance L is given by:

$$\begin{aligned} P_{\alpha\to\beta} &= |\langle\nu_\beta|\nu_\alpha(L)\rangle|^2 \\ &= \delta_{\alpha\beta} - 4\Sigma_{i>j} Re(U^*_{\alpha i}U_{\beta i}U_{\alpha j}U^*_{\beta j}) sin^2(\frac{\Delta m^2_{ij}L}{4E}) \\ &+ 2\Sigma_{i>j} Im(U^*_{\alpha i}U_{\beta i}U_{\alpha j}U^*_{\beta j}) sin(\frac{\Delta m^2_{ij}L}{2E}) \end{aligned} \tag{1.11}$$

where $\Delta m^2_{ij} = m^2_i - m^2_j$ (with m_i the neutrino masses). This formula is valid for any number of neutrinos, where U is the unitary leptonic mixing matrix, see equation 1.10.

As can be found in table 1.2 the Δm^2_{ij} values have been measured. For the neutrino masses, only upper boundaries have been established, these can be found in table 1.1. One of the big questions in neutrino physics is the ordering of the masses, the so called mass hierarchy. As shown in figure 1.3 there are two possibilities for the ordering: 1-2-3, the normal hierarchy, or the cyclic permutation 3-1-2, the inverted hierarchy [19].

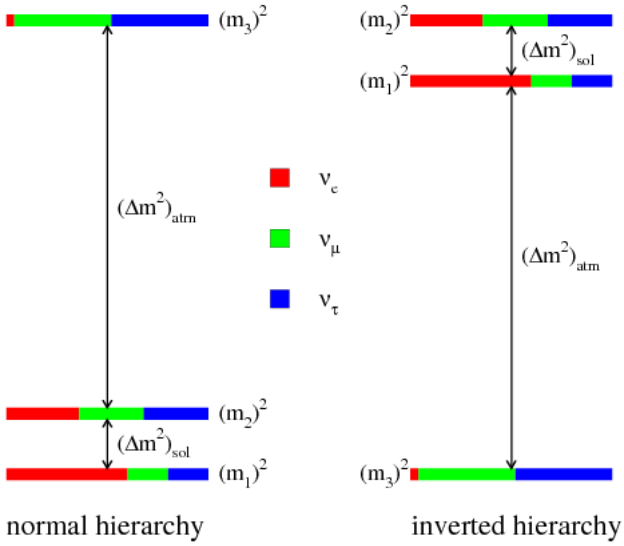

Figure 1.3: The normal and inverted mass hierarchy, where $\Delta m^2_{atm} = |\Delta m^2_{32}| \approx |\Delta m^2_{31}|$ and $\Delta m^2_{sol} = \Delta m^2_{21}$ [20].

[1] CP symmetry means that when a particle is interchanged by its antiparticle (C symmetry) and when the spatial coordinates are inverted (P symmetry) the fundamental laws of physics should be the same [18].

Table 1.2: Neutrino oscillation parameters. For Δm^2_{31}, $sin^2\theta_{23}$, $sin^2\theta_{13}$ and δ the upper (lower) row corresponds to the normal (inverted) neutrino mass hierarchy [21].

Parameter	Best fit	1σ range
$\Delta m^2_{21}[10^{-5}eV^2]$	7.62	7.43-7.81
$\Delta m^2_{31}[10^{-3}eV^2]$	2.55	2.46-2.61
	2.43	2.37-2.50
$sin^2\theta_{12}$	0.320	0.303-0.336
$sin^2\theta_{23}$	0.613	0.400-0.461
	0.600	0.569-0.626
$sin^2\theta_{13}$	0.0246	0.0218-0.0275
	0.0250	0.0223-0.0276
δ	0.80π	0-2π
	-0.03π	0-2π

Equation 1.11 is already very complicated to write down when one considers 3 neutrino flavors. Luckily there are some important situations in which we can make the approximation of only 2 neutrino types oscillating into each other. This happens in cases where a certain lepton is created that couples only significantly to 2 mass eigenstates that are related to a certain neutrino flavor. This is due to the smallness of the mixing angle θ_{13} and the mass difference Δm^2_{12}, see equation 1.2. Therefore, a simpler mixing matrix can be used:

$$U = \begin{pmatrix} cos\theta & sin\theta \\ -sin\theta & cos\theta \end{pmatrix}$$

There is also only one mass splitting Δm^2 to be considered. This then results in an easier formula for the oscillation probability:

$$P_{\alpha\to\beta} = sin^2(2\theta)sin^2(\frac{\Delta m^2 L}{4E}) \tag{1.12}$$

The two important situations where the 2 neutrino oscillation is often used, are that of solar and atmospheric mixing. Where one considers respectively the oscillations $\nu_e \leftrightarrow \nu_x$ (where ν_x is a superposition of ν_τ and ν_μ) and $\nu_\mu \leftrightarrow \nu_\tau$.

In 1998 the Super-Kamiokande Collaboration announced the first results that were consistent with neutrinos having a non-zero mass [22]. They did this by measuring the amount of muon neutrinos entering the detector from above and below. They found that there are less neutrinos coming from below, as they need to traverse the Earth instead of only the atmosphere. While traveling through the Earth the muon neutrinos can, according to the Super-Kamiokande team, oscillate into tau, or sterile (see next section) neutrinos. These data provided the first firm proof of the mass and the oscillation of neutrinos.

The Standard Model does not incorporate non-zero masses for neutrinos, so the previous findings open possibilities for new physics. For example, one or more sterile neutrinos could exist. These are called sterile as they do not interact weakly, this in contrast to the active neutrinos which are the kind of neutrinos mentioned up to now. If the sterile neutrinos would be able to interact via the weak force, they would couple to the Z boson, thereby increasing the width of its mass distribution. As seen in figure 1.2 there are only 3 neutrino flavors coupling to the boson, so any additional type should not interact weakly. The existence of such a sterile neutrino could provide an explanation for the smallness of the neutrino masses (see table 1.1 for upper limits) via the seesaw mechanism [23]. In this theory the sterile neutrino would then be a heavy counter particle to the light, known neutrinos. With the addition of a sterile neutrino, the Pontecorvo-Maki-Nakagawa-Sakata matrix, shown in equation 1.10, could be extended to a 4×4 matrix.

1.4 Neutrino anomalies

The picture of three flavors of neutrinos oscillating into each other is quite well accepted nowadays and it is supported by a lot of experimental evidence. However, there are a few results which are not consistent with this relatively well understood picture. These unresolved issues are called the neutrino anomalies.

The first experiment to observe a feature that is not compatible with the existing picture of 3 oscillating neutrinos was the LSND experiment in 1996 [24]. They investigated the oscillation of $\bar{\nu}_\mu \to \bar{\nu}_e$ by using neutrinos coming from the decay of μ^+ and detected the $\bar{\nu}_e$ through interactions with protons in the detector material. They observed a $3.8\,\sigma$ excess of electron antineutrinos. At the fixed distance L and energy E used in this experiment, an explanation for these data could be a larger mass difference between two neutrino species, see formula 1.12.

As the data of the LSND experiment were not confirmed by other experiments, the MiniBooNE experiment was designed to resolve the anomaly. The same L/E ratio was used as in the LSND experiment so that it was possible to compare the data. They conducted searches for $\bar{\nu}_\mu \to \bar{\nu}_e$ and $\nu_\mu \to \nu_e$ [25]. In the last case there was no excess reported in the energy region above 475 MeV, but there was evidence for a $3.0\,\sigma$ excess below this energy. In the case of antineutrinos an excess similar to the one observed in the LSND experiment was found.

Not only accelerator but also radioactive source experiments point towards a problem. The SAGE [26] and GALLEX [27] experiments were built to detect solar neutrinos and measure their corresponding flux, both consisting of a gallium detector. To conduct calibrations, radioactive sources (^{51}Cr and ^{37}Ar) are placed inside the detectors. In the

calibrations of both gallium experiments, a deficit of neutrinos coming from the sources was measured, see figure 1.4. The combined effect of the two experiments gives a 2.7 σ effect [28]. When one includes the large uncertainty on the cross-sections of neutrinos with the detector, there still remains at least a 1.8 σ deficit. The remaining effect could be explained by short-baseline oscillations of ν_e to a type of neutrino that cannot be detected.

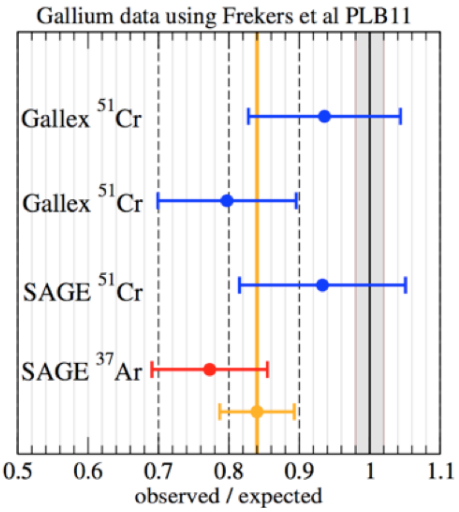

Figure 1.4: The observed deficit of neutrinos in radioactive source experiments [29].

The third kind of experiments that indicate there's something wrong with our picture of neutrinos are the nuclear reactor experiments. In these experiments the ratio R of the observed and calculated (under the hypothesis of 3 oscillating neutrinos) $\bar{\nu}_e$ flux is being measured. Recent evaluation of reactor neutrino fluxes indicate that the mean flux is increased by 3.5%. The combination of results from experiments with reactor-detector distances smaller than 100 m (short-baseline) gave a value of R=0.976±0.024, with the updated value of the flux this dropped down to R=0.943±0.023. This means that there is currently a deviation from unity at 98.6%C.L., which is called the reactor antineutrino anomaly [30].

There are several possible explanations for this anomaly. The first one is an incorrect prediction of the antineutrino flux. These calculations are very difficult as one needs to take into account the decays of many fission products present in the reactor core. Another cause of this deviation from unity could be a correlated artifact in the experiments. This seems unlikely as most of the experiments (Bugey-3, ROVNO91, Goesgen, ILL, ...) used either different detection techniques with varying features or different reactor fuels. A third possibility is that the anomaly is caused by a real physical effect, for example the existence of a sterile neutrino. In this case the electron antineutrinos could oscillate into a sterile neutrino, due to which they are not detected. Oscillations to muon or tau neutrinos cannot be possible causes of the anomaly as these effects are negligible at such

short distances. Solar and atmospheric oscillations can be neglected for distances lower than, respectively, a few kilometers and 100 m.

G. Mention et al. conducted research evaluating the compatibility of the data obtained by the reactor, radioactive source and MiniBooNE experiments with the existence of a single sterile neutrino [30]. The no-oscillation case is disfavored at the 99.8%C.L.. A combined fit gives rise to the following oscillation parameters: $|\Delta m^2_{new}| > 1.5\, eV^2$ (95%C.L.) and $sin^2(2\theta_{new}) = 0.14 \pm 0.08$ (95%C.L.). In figure 1.5 the agreement between the different hypotheses and the reactor data are displayed, where it is clear that in the region of small distances the difference between the two hypotheses is most distinct.

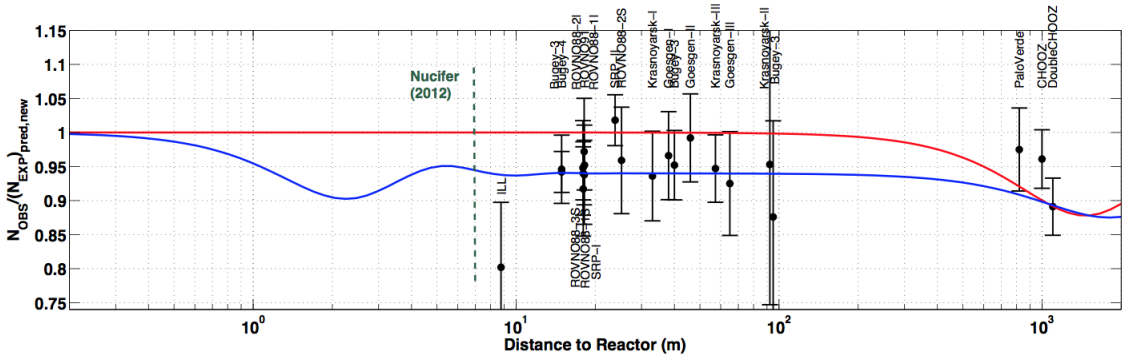

Figure 1.5: The reactor antineutrino anomaly. The red line shows a 3 active neutrino mixing solution fitting the data, with $\sin^2(2\theta_{13})$=0.15. The blue line displays a solution including a new neutrino mass state, with $|\Delta m^2_{new}| \gg 2\, eV^2$ and $\sin^2(2\theta_{new})$=0.12, as well as $\sin^2(2\theta_{13})$=0.085 [31].

With all these results, it becomes necessary to finally confirm or exclude the existence of a sterile neutrino. This can be done by building a very short-baseline reactor experiment or with a radioactive source experiment that has a good spatial and energy resolution. The advantage of the reactor experiment is the extremely high neutrino flux close to the core, about 10^{20} $\bar{\nu}_e$ per gigawatt per second. This allows for a compact detector and short measurement periods. One of the short-baseline experiments that would be able to measure the antineutrino energy spectrum is the SoLid project.

Chapter 2

SoLid

2.1 The SoLid Collaboration

SoLid is an experiment proposed by the university of Oxford and is short for "Search for oscillation with a ^{6}Li detector". The SoLid collaboration exists out of researchers attached to the University of Oxford, Imperial College London, SubaTech in Nantes and the universities of Ghent, Antwerp and Brussels.

The site of the experiment is the BR2 research reactor at the SCK•CEN at Mol in Belgium. This location was chosen for its superior features compared to other existing reactors. For example the distance of closest approach can be as small as 5.5 m, see figure 2.1. This is advantageous as the anomaly can best be investigated for small distances where the predictions for the ratio R for the different hypotheses (3 oscillating neutrinos or the 3+1 sterile neutrino case) are most differentiated, as can be seen in figure 1.5. Another advantage of the BR2 reactor are its good background conditions. As there are no other experiments being conducted on the same level as that of SoLid, all the other experimental ports facing the core are shut so that shielding is very effective. During the planned measurement period at BR2, SoLid will have the floor to itself so that there will be no change in conditions. This will avoid complication of the background evaluation. The reactor core of BR2 is very compact, 50 cm diameter $\times$ 90 cm, which makes it an effective, nearly point-like, source of antineutrinos. It also has a variable high power of about 45 to 70 MW. The reactor is running about 140 days per year and there is no time limit for the measurement period of the SoLid experiment.

The SoLid experiment will have a very high sensitivity to the oscillation under investigation. With the knowledge of the $\bar{\nu}_e$ flux, spectrum and the reactor-detector distance one can evaluate the hypothesis of an active to sterile neutrino oscillation according to formula 1.12. When the collaboration would be able to establish the existence of a sterile neutrino, this would be an extraordinary discovery in particle physics. It would have consequences for a lot of different research areas. On the other hand, if a sterile neutrino would not

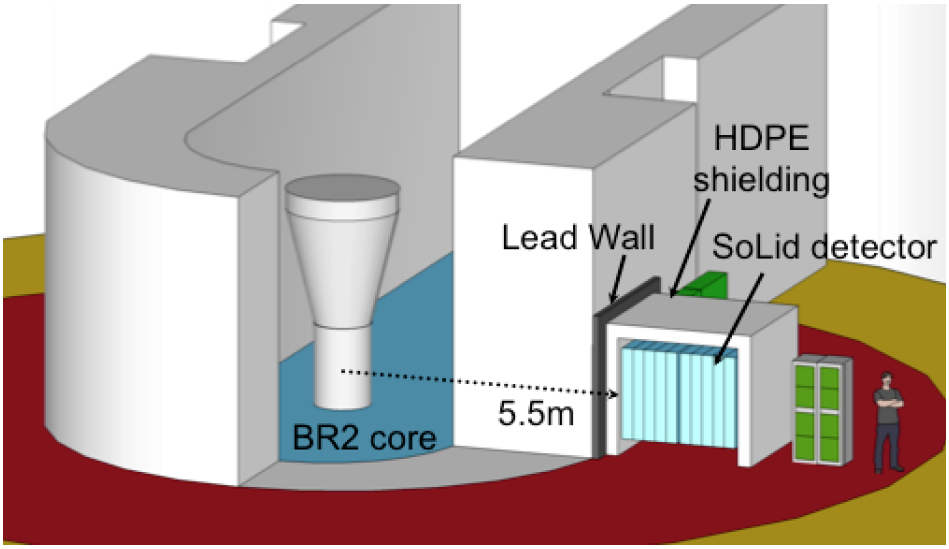

Figure 2.1: Sketch of the SoLid configuration at BR2 [32].

be found during the measurement period, an improved upper limit on its existence would weaken, or even eliminate, the sterile neutrino as an explanation for the anomalies discussed in section 1.4.

2.2 The detector technology

As in most cases, the electron antineutrinos will be detected by making use of the inverse beta decay, see equation 1.3. Hereby the antineutrino interacts with a proton of the detector thus creating a neutron and a positron. These last 2 particles need to be detected to make sure the signal is due to a antineutrino interacting in the detector. The SoLid detector uses detector technologies developed by the MARS project. The detector consists out of 5 cm × 5 cm × 5 cm cubes PVT scintillator[1] material covered with ^{6}LiF:ZnS(Ag) screens. These cubes, seen in figure 2.2, are individually wrapped in Tyvek, a type of synthetic paper, to ensure that the cubes are optically isolated from each other.

The positron created by the antineutrino interaction will immediately cause scintillation light in the PVT cubes, the neutron will be captured by the ^{6}Li sheet which has a very high cross-section for neutron interactions. This interaction:

$$^{6}_{3}Li + n \rightarrow ^{2}_{4}He(2.05MeV) + ^{1}_{3}T(2.75MeV) \tag{2.1}$$

will give rise to the excitation of ZnS energy levels due to collisions with the tritium and alpha particles. The de-excitation of these levels will give rise to scintillation light. The

[1] A scintillator is a material in which part of the kinetic energy of the incoming particle is absorbed and reemitted in the form of scintillation light [33].

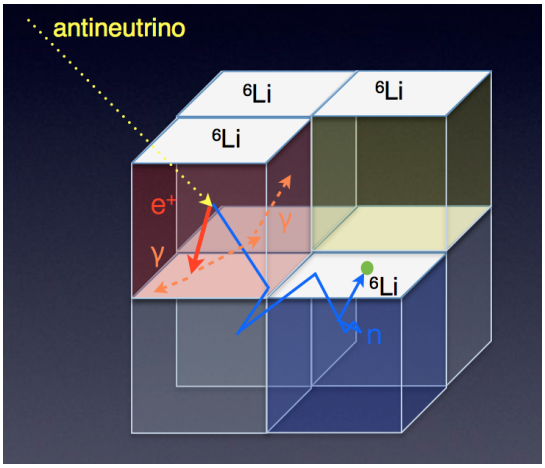

Figure 2.2: Configuration of the scintillator material and the ^{6}Li screens in the SoLid detector. An antineutrino reaction is shown [32].

energy levels have quite large decay constants, leading to a tail in the neutron signal, see figure 2.3.

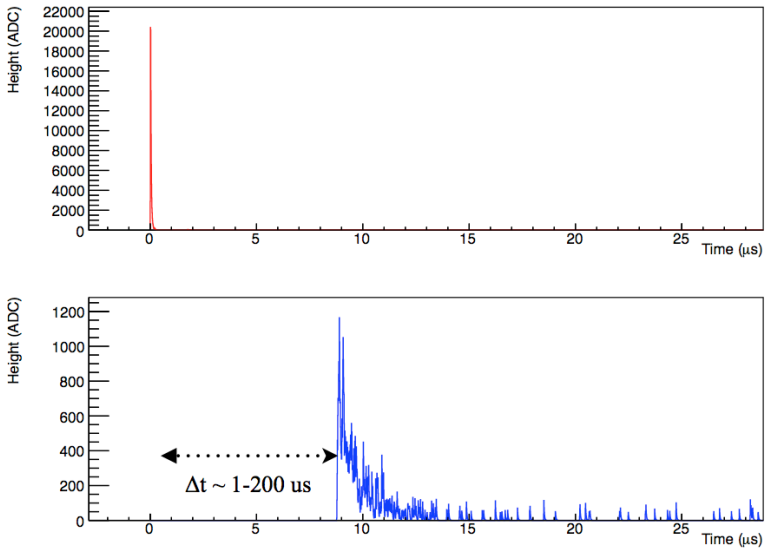

Figure 2.3: Signal due to the positron (top) and neutron (bottom) capture [32].

The positron will be captured approximately within 1 cm of the interaction and the neutron should stay contained within 15 cm (based on simulations, see [32]). The antineutrino signal is thus relatively well confined around the interaction point compared to the dimensions of the total detector. This would create an extra tool in the discrimination against background. In figure 2.4 a typical inverse beta decay (IBD) event can be seen.

The scintillation photons created by the interaction of the antineutrino are collected by

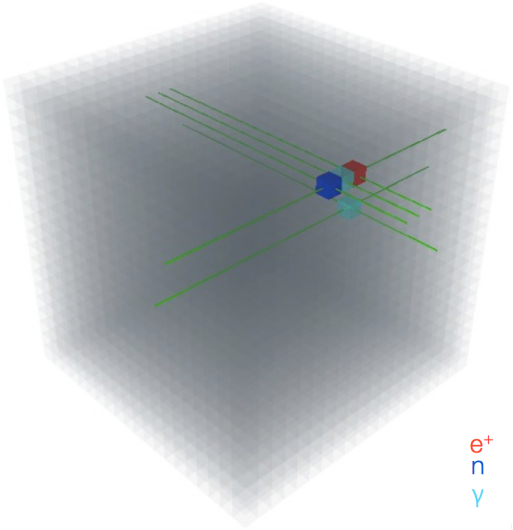

Figure 2.4: Simulation of an IBD event [32].

wavelength shifting[2] fibres which are coupled to multi-pixel photon counters (MPPCs), also known as a silicon photomultipliers, where the signal is read out. This happens in the vertical and horizontal direction (see figure 2.5), which gives very good position information as in this way one can determine in which cube the light was created and thus collected. The operating principle of a photomultiplier will be explained in section 3.1.

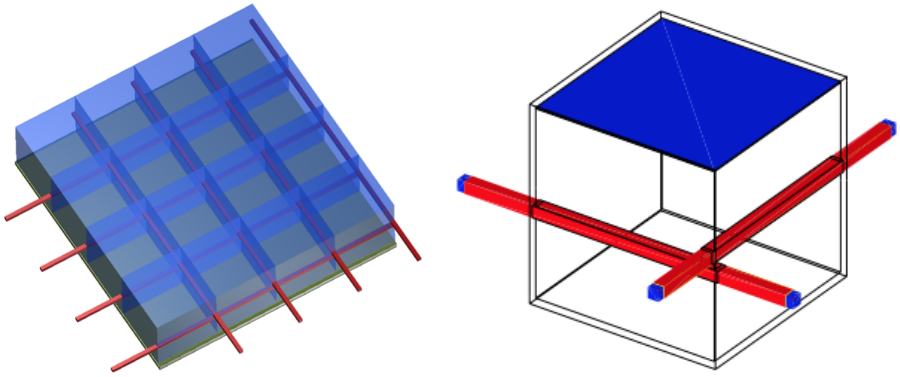

Figure 2.5: Configuration of the fibres [32].

It is impossible to measure the energy of the interacting neutron as it thermalises before it is captured by the ^{6}Li screen. The energy of the positron however, can be measured by collecting all the emitted scintillation light. One can convert the signal read out at the MPPCs into the positron energy with the knowledge of the detector efficiency.

[2]A wavelength shifter is a material which absorbs the primary scintillation light and reemits it at a longer wavelength. It is used to match the spectrum of scintillation light with the efficiency spectrum of the PMT. This is necessary as a PMT is not equally efficient for different wavelengths [33].

This can then be used to give a probability distribution of the interacting antineutrino's energy and ultimately of the antineutrino spectrum after measuring a large number of events.

The SoLid detector will be composed out of different modules that consist out of several aluminum frames each filled with 256 cubes. The total detector will consist out of thousands of cubes. The different modules can be placed at different distances from the reactor core and thus one can get information about the oscillation parameters that is less dependent on the complicated antineutrino flux calculations. The detector modules themselves will be placed inside a high density polyethylene (HDPE) shielding to reduce background, especially neutrons, and increase sensitivity even more.

2.3 NEMENIX

To estimate the detection efficiency and to get a grip on possible construction and working problems, a prototype for the Solid detector was built. This prototype is called NEMENIX and uses the same detection principle and materials as discussed in section 2.2 for the SoLid detector. It consists out of 64 cubes and its dimensions are about 20 cm × 20 cm × 20 cm, see figure 2.6. There are 32 read out channels and an HDPE shielding which has a thickness of 20 cm.

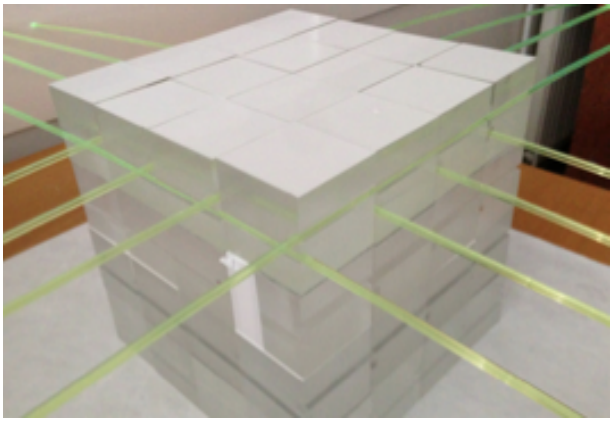

Figure 2.6: The NEMENIX detector [32].

The detector was installed at the BR2 site in Mol in the summer of 2013. It is placed at a distance of 5.5 m away from the reactor core and it is situated in the same location as that planned for the SoLid detector, see figure 2.7. The first data were taken in August 2013 and the detector is currently, May 2014, still running during reactor off- and on-cycles.

Building the NEMENIX detector and taking data should give a very good idea of unsolved mechanical, technical and DAQ problems. It should also give an indication of how

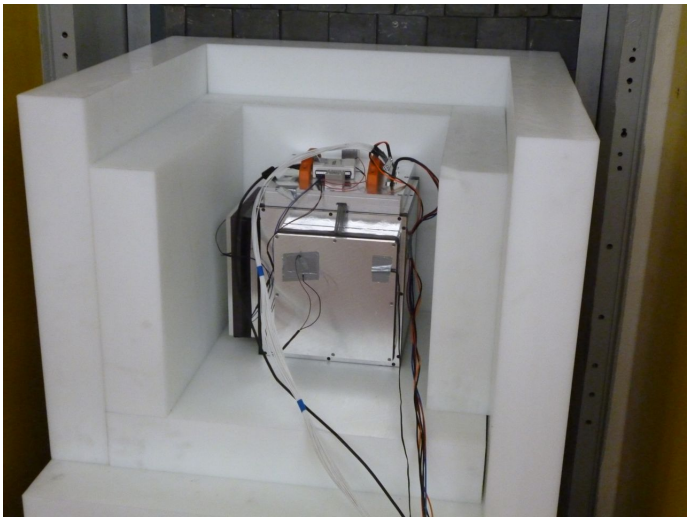

Figure 2.7: The NEMENIX detector at the BR2 site, in the (open) HDPE shielding and with cables for readout visible [32].

good the efficiency of the detector will be and whether the position and energy resolution will be good enough to be able to investigate the short-baseline oscillation. In any case, the NEMENIX prototype will give very useful insights for the construction of the SoLid detector and for the data taking stage which will start in November 2014.

2.4 Background evaluation

Like most neutrino experiments, the SoLid experiment requires a very sensitive measurement. Therefore the influence of background needs to be eliminated as much as possible. In a lot of experiments involving neutrino detection, the detectors are placed at large depths underground. Such as the Super-Kamiokande experiment, discussed in section 1.3, which is located in the Kamioka Mine in Japan at a depth of 1000 m [34].

Locating experiments deep underground, in a mine, under a mountain, or even in ice or water, provides a very effective shielding for cosmic rays[3]. Although in most cases one still needs to take the influence of atmospheric muons into account as these particles can penetrate quite some distance underground.

The SoLid experiment, and the NEMENIX prototype, are located at the BR2 reactor which is situated above the ground. There is no real shielding from muons, except for the

[3]Primary cosmic rays are very energetic particles, mostly created outside of our solar system. When they impinge on the earth's atmosphere they create secondary cosmic rays, which are mostly neutrons, pions and kaons. The pions can then decay into muons which are able to reach the surface of the earth [35]. These atmospheric muons represent a significant background for most neutrino experiments.

concrete walls which are part of the containment building surrounding the reactor. It is thus very important to evaluate the influence of these muons. One needs to get an idea of the signals which are produced in the detector by passing muons. The installation of extra detectors to establish the passage of a muon, should also give a way to separate the muon signals from the neutrino signals we are looking for. How this is done will be discussed in chapters 3 and 4 and it forms the subject of this thesis.

Aside from the muon signals, one also needs to take into account the fast neutrons, which are generated in the fission processes that take place in the reactor core. A first shielding from neutrons is provided by the lead wall that is situated at the experimental port that separates the NEMENIX detector from the core. An extra shielding is provided by the HDPE box around the detector itself. Neutrons that are still able to reach the scintillator can give a signal. However, it should be possible to reject these events as there is a coincidence required between a fast and a slow signal to simulate a neutrino event, see figure 2.3. A different situation arises when the neutron signal is preceded by a gamma signal within the time window which we would expect for the neutrino interactions. These are called "coincidentals". With the help of detector simulations one can develop good spatial and timing cuts which can reduce this kind of background substantially.

The data-taking with NEMENIX and the extra muon detectors, as well as the background simulations will give useful insights into the rejection capabilities of the detector and the background differences during reactor-off and -on periods.

Chapter 3

Muon detection for NEMENIX

A careful background evaluation is necessary when one wants to perform a sensitive measurement such as that of the short baseline oscillations. One of the backgrounds are the atmospheric muons, as mentioned in section 2.4. These are very penetrating particles with energies on the GeV scale and they can hardly be stopped by the HDPE shielding available at NEMENIX. Therefore it is of paramount importance to get a grip on the properties of the signals that muons create in the NEMENIX detector. This can be done in 2 separate ways. One could have a look at the simulation of muons in the detector. A second approach is to investigate the data itself, see chapter 4.

As it might not be possible to distinguish muon signals from other background signals, or even from the real anti-neutrino signal with only the compact NEMENIX detector, extra muon detectors are installed. The installation of these extra detectors might not be necessary in the complete SoLid detector as this detector consists out of a lot more cubes. One expects the muon to penetrate the whole detector and thus leave a, more or less, straight track. In the NEMENIX detector, which only has 64 cubes, this track is possibly not long enough to distinguish from other signals which can also comprise several cubes. Matching the muon signals in the muon detectors with signals in the NEMENIX prototype should give insight into how good the NEMENIX detector is at differentiating between muon and other signals.

3.1 Muon detection planes

The muon detection planes, which will serve as an extra tool in the identification of muon signals, were built at Ghent University. There are four muon detectors, 2 small and 2 large ones. The small and large detectors respectively have the following dimensions: 35 cm $\times$ 35 cm $\times$ 1,4 cm and 70 cm $\times$ 70 cm $\times$ 1 cm. They are made out of BC300, an organic scintillator material. On the side of the scintillator planes a wavelength shifting bar is coupled with optical silicon gel. The wavelength shifter is somewhat longer than the muon plane and has a square cross-section of 1 cm $\times$ 1 cm. The whole, plane plus bar, is wrapped in

aluminum foil. On one end of the wavelength shifting bar a photomultiplier tube (PMT) is coupled, again with optical gel. A connecting piece is used to make sure that the PMT stays in contact with the bar.

A photomultiplier tube is responsible for the conversion of a scintillation light pulse into an electrical signal. The PMT consists out of an outer, in this case glass, envelope. There is a vacuum in the tube so that low-energy electrons can be accelerated efficiently without losing energy by colliding with gas atoms. The most important parts of the tube are the photocathode and the electron multiplier structure, see figure 3.1. At the photocathode the impinging scintillation photons are converted into low-energy electrons. As there are typically so little electrons, the signal needs to be amplified before it can be used in practical situations. The electron multiplier serves to multiply the number of electrons in a linear way. This means that the output current is still a good representation of the energy of the original photon signal. In this way, a typical scintillation pulse will give rise to about 10^7-10^{10} electrons, which is sufficient for a practical charge signal [33]. The PMTs used with the muon planes give negative output pulses.

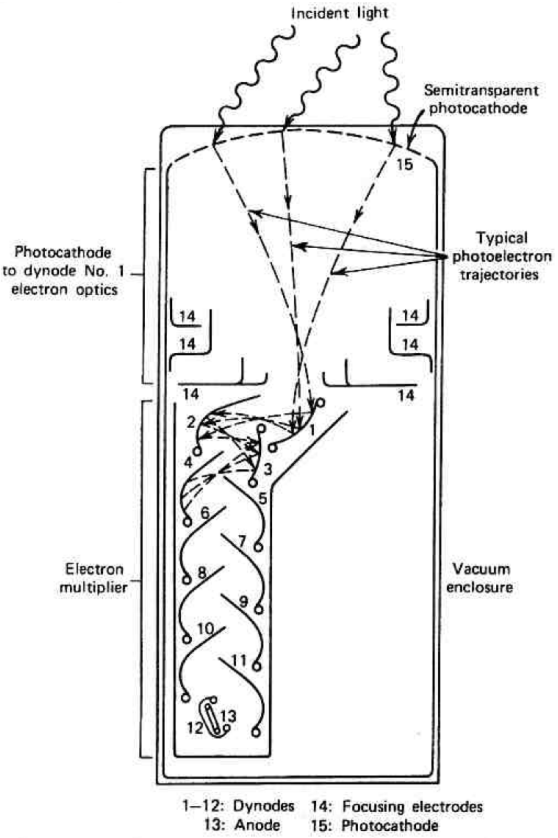

Figure 3.1: Basic elements of a PMT [33].

Originally the muon detectors were placed in black wooden crates to shield them from

light. However, wood is not allowed inside the containment building at the BR2 reactor due to contamination risk. Therefore the scintillators are removed from their encasements and, to make them light tight, they are wrapped with black plastic foil and secured with black tape. To test whether the detectors are sufficiently shielded from external light, the signals are investigated with an oscilloscope. There is no visible difference in the signals when the detector is covered with a heavy black cloth, which proves that the plastic foil is isolating enough.

3.2 Electronics

The electronics which are used in connection with the muon detectors are all nuclear instrumentation modules (NIM). NIM defines a standard in electronic modules which are used in nuclear and particle physics. This standard makes it easy to change the setup and replace modules. All the modules are placed inside a NIM crate which provides the DC power via the backplane [36]. All connections between PMT and electronics, except for the HV connection, and the linking between modules is done with LEMO, push-pull, connectors.

The muon detectors are powered by the ORTEC 478 high voltage (HV) modules. As there are only 2 power supplies available, there are 2 PMTs powered by the same HV module. As this means that these 2 PM tubes are necessarily at the same voltage, 1 power supply is connected to 2 detectors of the same size.

The signal of the large detectors without an amplifier is somewhat weaker than that of the small ones. This is to be expected as the scintillation light collection is not perfect and an event occurring further away from the PMT gives a weaker signal. This maximal distance can be a lot bigger in the large than in the small detectors. To accommodate for this effect the signals coming from the large planes pass through a LECROY 612a amplifier before entering the rest of the electronic circuit. This module has a linear gain of a factor 10.

The signals then enter a linear fan-in/fan-out, CAEN N401, which takes care of generating multiple outputs from one input. In this way it is possible to investigate the signal of the PMT with an oscilloscope, while still being able to use the same signal as an input for another module.

The other output of the fan-in/fan-out serves as input for the ORTEC 935 constant fraction discriminator (CFD). This module converts the linear PMT signals into block, or logic, pulses if they exceed a certain voltage threshold. The correct value of this threshold is found by performing an efficiency measurement which will be explained in section 3.3. The width of the block pulse can also be adjusted. Here, a value of 100 ns is chosen as this is required by the scaler, see later in this section. The principle of a constant fraction

time pick-off method is shown in figure 3.2 [33]. A time pick-off method or trigger is the generation of a logic pulse whose leading edge indicates the time of occurrence of a linear input pulse. The zero-crossing time that is obtained in plot (d) is the time at which the output is generated, this point is independent of the pulse amplitude for pulses with the same shape. This way of triggering reduces the uncertainty in deriving the timing signal and is applicable to scintillator signals. The delay time t_d, which is shown in plot (c), is provided by inserting delay cables in the delay input of the module. This delay time should be larger than the width of the PMT signal. A delay of 30 ns proved to be sufficient after the investigation of the signals on the oscilloscope.

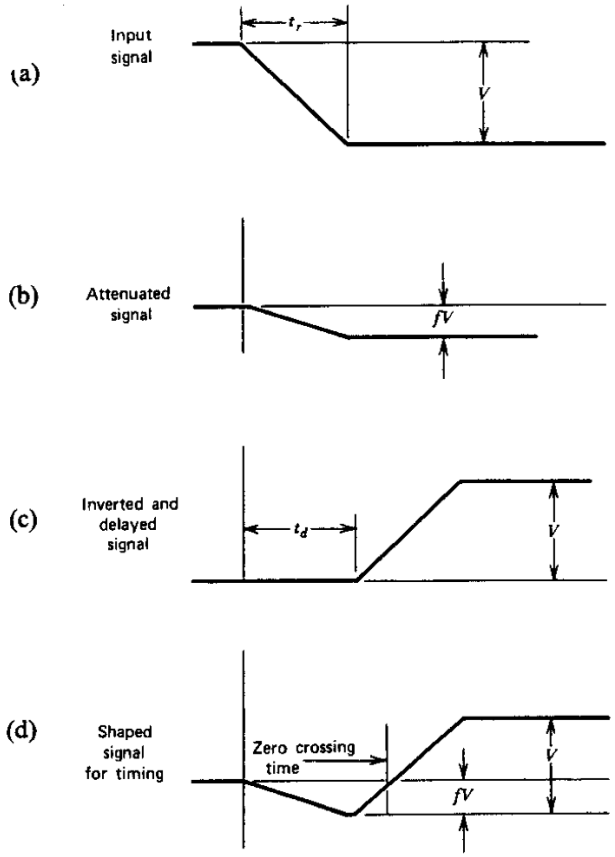

Figure 3.2: Waveforms in the constant fraction time pick-off method. Only the leading edge of the pulse is shown [33].

After the PMT signals are transformed into logic pulses by the CFD, they pass by the LECROY 622 coincidence module. This module provides a logic pulse as output when there are 2 logic input pulses within a certain time window τ, when the AND condition is selected. In this setup τ is 100 ns as it is given by the width of the input signals.

The coincidences of the PMT signals should be counted and displayed. This is done by a scaler, also called counter, which was made in Ghent. It is quite an old module which is not

compatible with the NIM signals coming from the corresponding modules. Instead it uses TTL signals. To accommodate for this, a PEGEL converter is used which converts a NIM into a TTL signal. This can then be used as an input for the scaler. During the measurements it became clear that the scaler needs rather wide signals as an input or otherwise does not count all the input signals. Therefore the width of the logic pulses was chosen to be 100 ns, which proved to be sufficient as further increasing this width did not raise the number of counts. The scaler has 3 displays which makes it possible to count 3 different signals during the same measurement. The counting can be regulated with the start, stop and reset button. During several measurements the stop button did not function and thus the measurement needed to be stopped by switching the HV power supplies of the PMT off.

In figure 3.3 the electronic setup used in Ghent is shown. This identical setup is presently, May 2014, installed at the BR2 reactor.

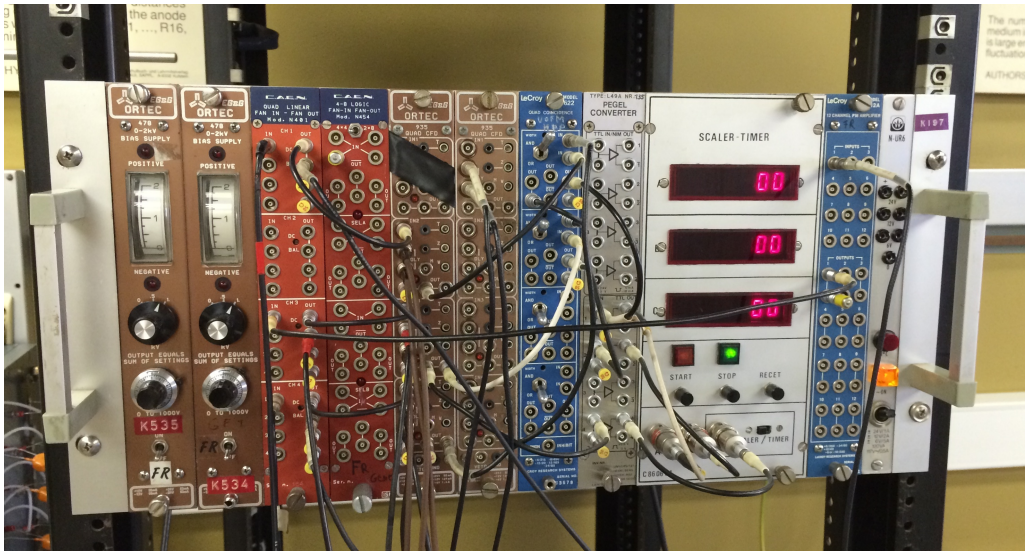

Figure 3.3: The NIM crate with the electronic modules used in the measurements. Starting from the left, there are 2 HV modules, the linear fan-in/fan-out, a logic fan-in/fan-out (which is not used), 2 CFDs (of which one is not used), the coincidence module, the converter, the scaler and the amplifier.

3.3 Efficiencies of the muon detectors

It is not possible to build the perfect detector that can detect all passing particles. In a lot of different stages something can go wrong so that the passing muon can not be detected. For example the scintillation efficiency[1] of the detector can be lower at some places due

[1]The scintillation efficiency is the fraction of incoming particle energy that is converted into photon energy.

to the presence of defects. The optical connections between the scintillator and the wavelength shifting bar and between the wavelength shifter and the PMT can be non-optimal whereby not all the scintillation light is collected. The quantum efficiency[2] of the PMT is also an important factor in the efficiency of the total detector. All these effects can cause the signal to be reduced so that it no longer passes the threshold set by the CFD, see section 3.2. It is thus clear that in practice not all events will be detected. Of course it is very important to know which fraction of the events is seen by the detector, this quantity is called the efficiency of the detector. In most cases the efficiency is measured for the detector, PMT and electronic circuit together.

In the context of this thesis, the efficiencies of the 4 muon planes are measured. Also here, the efficiencies of the PMT and electronic modules are included. To determine the fraction of detected events, the muon detector under investigation is placed between 2 other muon planes. When a muon passes and gives a signal in the upper and lower detector it should also have passed the middle detector and therefore also the middle detector should give a signal. As mentioned in section 3.2 the coincidence unit in the NIM crate can determine whether 2 signals are detected within a certain time from each other with the AND operation. When this is the case, a coincidence is counted. In the efficiency setup, the signals of the upper and lower detector are checked for coincidences. The output of this operation serves as input, together with the signals from the middle detector, for a second coincidence AND operation. In this way one can keep track of the number of coincidences between the upper and lower detector and the coincidences between all 3 detectors. The results are displayed on the scaler. Showing these 2 numbers leaves the possibility to also display the number of signals in a specific detector, the so called single counts. In these measurements it was chosen to display the number of signals from the middle detector. A schematic representation of the electronic circuit is shown in figure 3.4, here Muon 1, 2 and 3 correspond respectively to the upper, middle and lower detector in the efficiency setup.

To make it easier to keep the 2 small and the 2 large detectors apart, one of each is labeled with red tape on the plastic foil near the PMT. As the efficiencies of the detectors are different, even for the same size, it is necessary to be able to distinguish between the different detectors. Therefore the detectors are given names: small red (SR), small black (SB), large red (LR) and large black (LB). Where the colors red and black refer to the presence or absence of the red tape respectively. When it is necessary to refer to the position of the detector, the convention upper detector = 1, middle detector = 2 and lower detector = 3 will be followed.

Figure 3.5 shows the setup which is used in the measurement of the efficiencies. On the

[2]The quantum efficiency of a PMT is defined as the number of photoelectrons collected by the multiplier structure per incident photon on the photocathode [37].

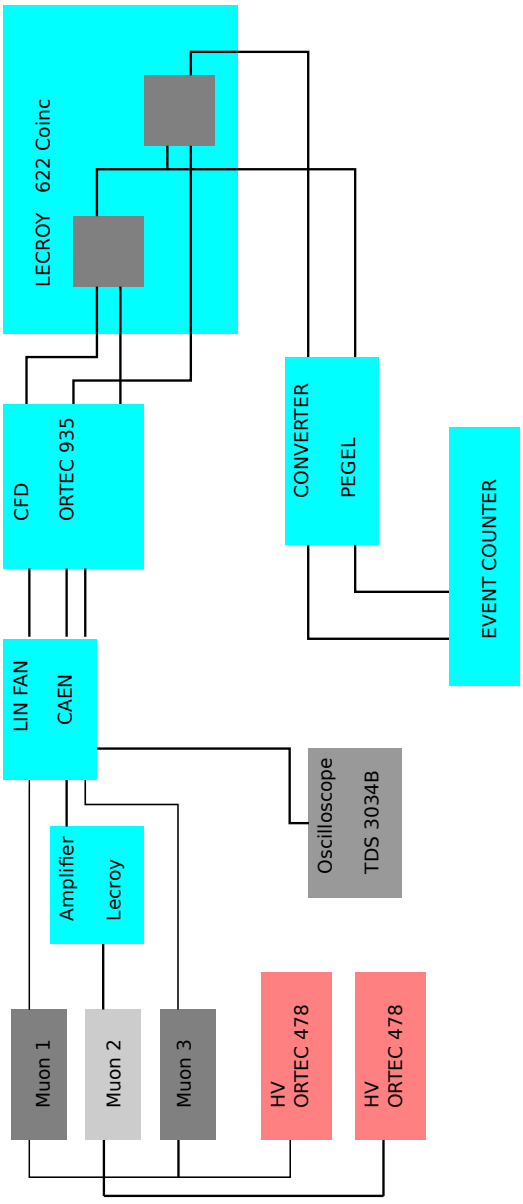

Figure 3.4: Schematic representation of the electronic read-out for the setup in Ghent.

left plot the case of the small detectors is shown and on the right that of the large ones. As not more than 2 large detectors are available at Ghent, it is not possible to sandwich a large detector between 2 others so that its area is totally covered. Therefore the efficiency for the large detectors obtained in the following measurements is an overestimation, or in any case an upper limit, to the real efficiency as one has no knowledge of possibly broken areas of the large detector which were not covered by the small planes during the measurements. Variations in efficiency of the different regions of the large muon detectors are also unknown as the efficiency was only measured for one specific area of the large planes, see the right figure in 3.5.

When the efficiency of a small plane is measured one has to take into account that due to the geometry of the setup, it is possible that a muon passes through the upper and lower detector, but not through the middle one. This can be seen on the left side of figure 3.5. To estimate this effect, a MonteCarlo simulation is written in C++. In this code a random position on the surface of the upper detector is generated with the mt19937 pseudo random generator. With the same generator a random direction, (θ, ϕ), is obtained. As cosmic muons have a $\cos^2\theta$ angular distribution, this is taken into account in the program [2]. If the line defined by the initial position and direction crosses the middle or lower detector as well, this is counted as a coincidence. It is allowed to treat the path of the muon as a straight line as these particles are very energetic. In table 3.1 the results of the simulation can be found. As can be seen, 96.8 % of the events passing the upper (1) detector also pass through the middle (2) and lower (3) detector. The important quantity for the geometric efficiency is the fraction of coincidences between all 3 detectors (B) compared to the coincidences between 1 and 3 (A). Dividing B by A one gets a geometric efficiency of 96.85 %. To obtain the total efficiency of the small detectors, this quantity needs to be taken into account. As can be seen in figure 3.5, right figure, this calculation is not necessary for the efficiency measurement of the large detectors. Since the large (2) detector is sandwiched between small (1, 3) detectors it is geometrically not possible that the muon passes 1 and 3 without passing detector 2.

Table 3.1: The results of the geometric efficiency simulation.

Number of events	Coincidences between 1 and 3 (A)	Coincidences between 1, 2 and 3 (B)
1 000 000	999 390	967 995
Fraction passing through 1(%)	Fraction passing through 1 and 3 (%)	Fraction passing through 1, 2 and 3 (%)
100.00	99.94	96.80

Figure 3.5: The setup used to measure the efficiency of the small (left) and large (right) muon detectors.

As already mentioned in this section, the efficiency of detectors is measured by sandwiching the detector between 2 others and counting the number of coincidences between 1 and 3 (A), and 1, 2 and 3 (B). By dividing B by A one gets the efficiency of detector 2. This efficiency measurement is performed for different values of CFD threshold for the small detectors. For the large detectors it is done in function of high voltage as no efficiency plateaus were found during measurements in function of threshold.

In measuring the efficiency of the SR detector, SB = 1, SR = 2 and LB = 3 and all the PMTs are powered by 1.40 kV. The thresholds of SB and LB are respectively 65 and 75 mV. These values are chosen arbitrarily as the measurement of the SR detector is the first to be performed. The measurements at different SR threshold values have a duration of 5 minutes, except for the point at 30 mV which lasted an hour. The results, as well as the rate of SR during the measurement (single counts), can be seen in figure 3.6. The efficiency plateau is found from 18 to 41 mV and averaging over these data points gives an efficiency of 88.7±1.2 %. On the basis of these measurements a value of 30 mV is chosen for the threshold of the SR detector. It is a good value as it is well in the plateau region. It is low enough to reduce the noise and high enough to make sure small signals are still detected.

For the measurement of the SB detector, SR = 1, SB = 2 and LB = 3 and all the PMTs are again at a HV of 1.40 kV. The fixed thresholds of SR and LB are respectively 30 mV and 75 mV. Here the value for SR was determined during the previous measurement while the value for LB is still arbitrary. Except for the data point at 30 mV, which lasted 1.5 hours, all measurements again had a duration of 5 minutes. As can be seen in figure 3.7, the plateau is found between 26 and 40 mV and the averaged efficiency is 83.1±1.7 %. Again a threshold of 30 mV is chosen.

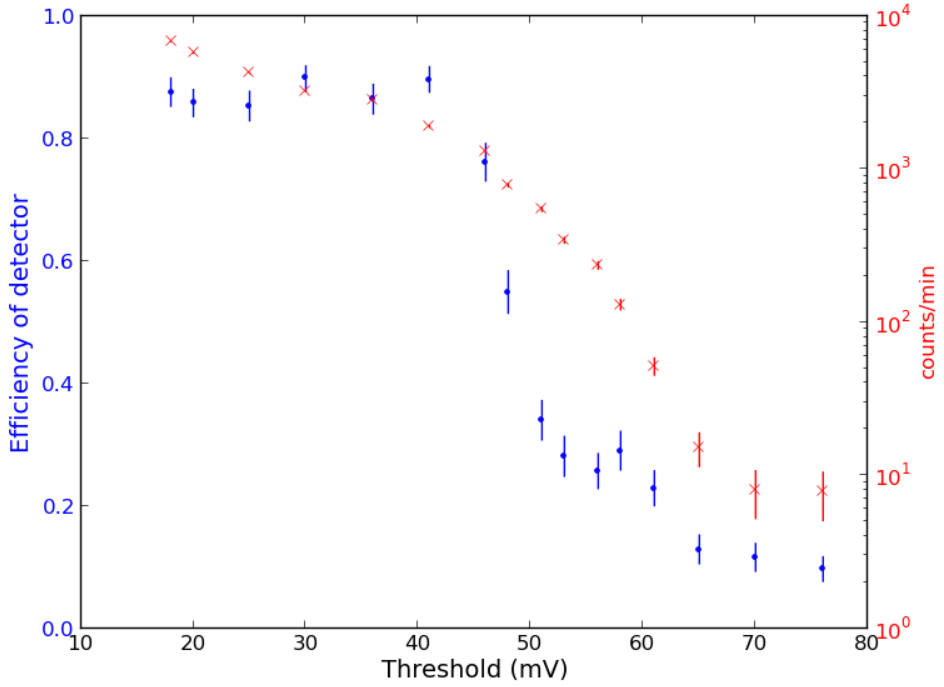

Figure 3.6: The efficiency (points) and single counts (x's) of SR in function of threshold.

The efficiency of the LR detector is measured in function of high voltage as a first measurement in function of threshold did not give any useful results and no efficiency plateau was seen. In this setup SR = 1, LR = 2 and SB = 3 and only SR and SB are at a fixed voltage of 1.40 kV. Now, all the thresholds are fixed at the values of 30 mV for the small detectors and 45 mV for LR. The thresholds for the small detectors were determined in the previous measurements. The threshold value of LR is found by performing the efficiency measurement for several descending values, starting from 65 mV, until an efficiency plateau is found. All measurements shown in figure 3.8 lasted for 5 minutes. The efficiency plateau is found from 1.40 to 1.55 kV and has a value of 84.1±1.0 %. A standard voltage of 1.40 kV is chosen as it should be kept as low as possible to maintain good operation of the PMT.

The last efficiency that is determined is that of the LB detector. Here SR = 1, LB = 2 and SB = 3 and SR and SB are at a fixed voltage of 1.40 kV. The thresholds are fixed at 30 mV for the small detectors and 50 mV for LB. The threshold values of the small detectors were determined in the previous measurements. The value of 50 mV for the LB detector is chosen according to the same principle that is used for the determination of the threshold value of LR, mentioned in the previous paragraph. The duration of the measurements is 5 minutes. The plateau in figure 3.9 can be found from 1.25 to 1.60 kV

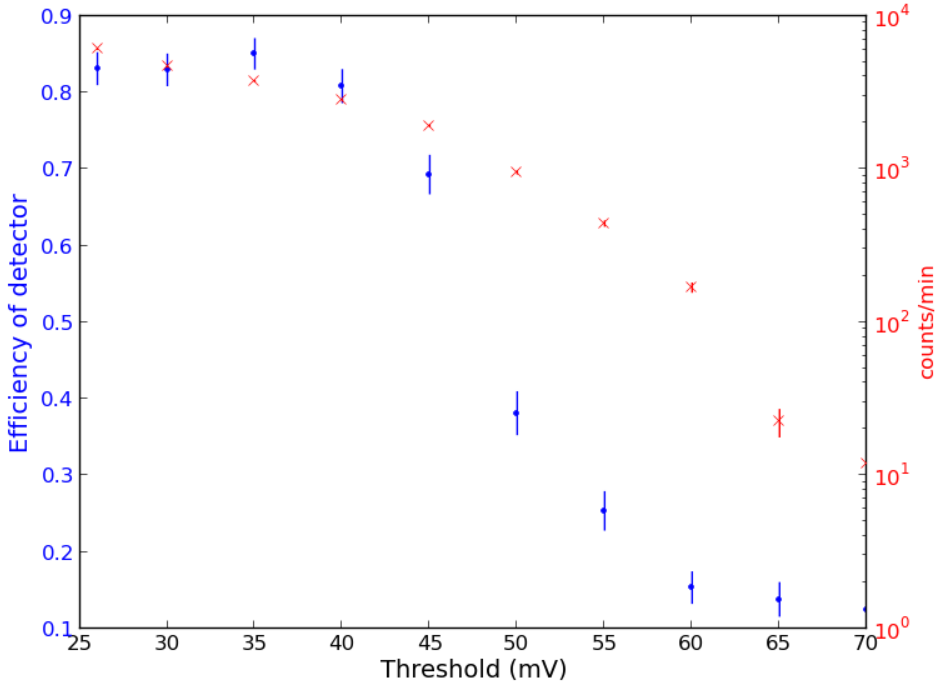

Figure 3.7: The efficiency (points) and single counts (x's) of SB in function of threshold.

and has a value of 79.9±0.9 %. As for the LR detector, a value of 1.40 kV is chosen for further operation. The HV power needs to be the same for the 2 large planes as these are powered by the same HV module. It is therefore convenient that the value of 1.40 kV is situated in the plateau region for both detectors.

It can be noticed in figures 3.6, 3.7, 3.8 and 3.9 that the single counts curve of the detector under investigation roughly follows the shape of the efficiency curve. This is to be expected as the single counts value should be coupled with the number of coincidences between detectors 1, 2 and 3. When there are more counts, due to a lower threshold or a higher HV, there should be more coincidences, and thus a higher efficiency. Of course this does not apply to the region where a lot of noise is counted. As can be seen in figure 3.8, the single counts curve shows a dip in the region of 1.5 kV. There does not seem to be a valid explanation for this and it could not be checked whether the curve goes up again as this would exceed the maximum voltage of the PMT.

In table 3.2 a summary of the measured efficiencies can be found. The values for the small detectors need to be corrected for the geometrical factor, due to which 3.2 % of the events giving a coincidence in detector 1 and 3 do not pass detector 2. The intrinsic efficiency of the detector can be found by dividing the measured efficiency by the geometric efficiency (96.85 %).

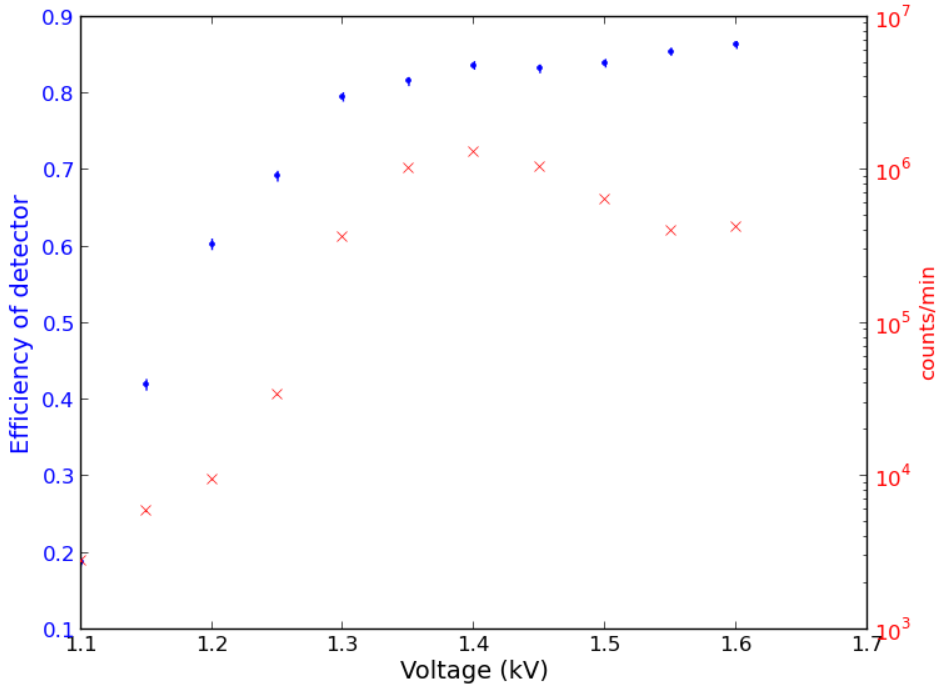

Figure 3.8: The efficiency (points) and single counts (x's) of LR in function of HV.

Table 3.2: Summary of the muon detector efficiencies.

Detector	Measured efficiency (%)	Error (%)	Corrected for geometry (%)
SR	88.7	1.2	91.6
SB	83.1	1.7	85.8
LR	84.1	1.0	-
LB	79.9	0.9	-

3.4 Installation of the detectors at BR2

After testing the detectors in Ghent and preparing them for operation at BR2 by removing them from their crates and wrapping them in black foil, see section 3.1, the detectors are ready for installation at the reactor. To be able to install the small detectors, the shielding of NEMENIX is opened and extra openings are drilled into the HDPE to allow passage of the read-out cables. The SB and SR detector are positioned in vertical position on respectively the left and right side of the NEMENIX prototype. The wavelength shifter and PMT are situated on the top side as to not add unnecessary pressure to the rather fragile connection between those 2 parts of the detector. The dimensions of the large muon planes

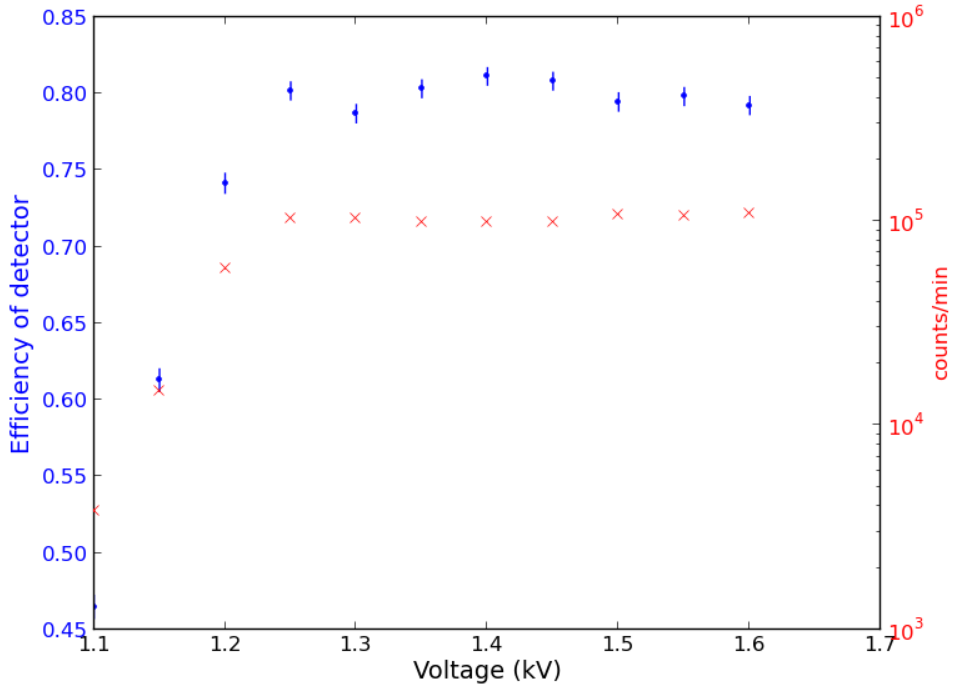

Figure 3.9: The efficiency (points) and single counts (x's) of LB in function of HV.

are to big to allow them to be placed on the inside of the shielding. Therefore the LB and LR detector are placed respectively on top and below the shielding. The LB detector rests on the top of the shielding, while the LR detector is placed on a shelf which is positioned between the legs of the table upon which NEMENIX is positioned. The setup can be seen in figures 3.10 and 3.11.

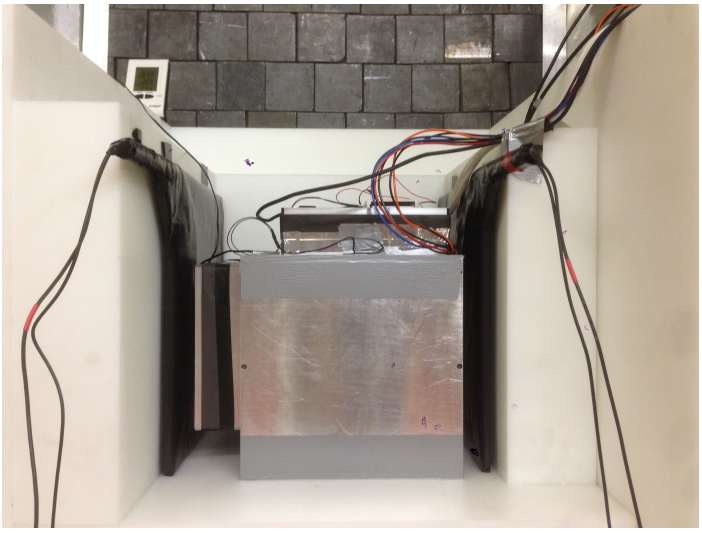

Figure 3.10: The NEMENIX detector with the SB (left) and SR (right) muon planes.

Figure 3.11: The NEMENIX detector with closed shielding and LB (top) and LR (bottom) muon planes.

The electronics that were used in the efficiency measurements in Ghent, described in section 3.2, are reused in the setup at BR2. The muon planes remain powered by the same high voltage modules and are maintained at a voltage of 1.40 kV. The signals from the large detectors are amplified as was done for the measurement of the efficiencies. Using an adaptor, the signal cable from the PMT is coupled with a LEMO to BNC adaptor to a BNC to MCX cable. The MCX connectors can be used as an input for the data acquisition system (DAQ) of NEMENIX. This DAQ is a VME (versa module Europa) system consisting out of 5 CAEN V1724 digitizer boards, labelled 0 to 4. Board 4 reads

the 4 channels corresponding with the 4 muon detectors. The other boards each read 8 channels coming from the NEMENIX detector. The digitization of the channels is done with an analog to digital converter (ADC) which has a range of 2.25 V and a bit resolution of 14 which means that 1 ADC count corresponds to $2.25\,\mathrm{V}/2^{14}$=0.14 mV. Each channel has a programmable offset of ± 1.125 V, so that the 2.25 V range can be adapted to the input signals. For the NEMENIX channels signal voltages between -0.125 V and 2.125 V are measured, as these signals have a positive polarity. As the muon plane PMTs give a negative signal, the range is set from for -1.125 V to 1.125 V. Apart from the digitizer boards, there is also a V2718 board present in the VME crate. This board collects data from each of the V1724s and sends it to the computer over an optical connection. In table 3.3 a summary of the muon detectors and their corresponding VME channel number can be found.

Table 3.3: Summary of the detector planes.

Detector	Position at BR2	HV (kV) at BR2	Cable nr.	VME channel
SB	left vertical	1.40	38	0
SR	right vertical	1.40	39	1
LR	below horizontal	1.40	40	2
LB	upper horizontal	1.40	41	3

Chapter 4

Analysis of muon signals

In view of distinguishing muon from other signals in NEMENIX, and later in the full SoLid detector, one wants to know as much as possible about the properties of the muon signals. This can be done by running simulations, but also by looking at data. Concerning muons, the goal is to be able to identify a muon signal in NEMENIX. Using the muon planes, it should be easier to establish the presence of a muon in the NEMENIX detector. When one observes a coincidence between signals in at least 2 muon detectors and at the same time observes a signal in NEMENIX, the signals are almost certainly caused by the passage of a muon. However, a muon passing 2 muon planes does not necessarily hit NEMENIX due to geometric reasons which will be discussed in section 4.3. Therefore the 2 important steps in investigating the muon signals are obtaining the properties of these signals as well in the muon planes as in NEMENIX and afterwards matching these signals as to establish the passing of a muon through the complete detector system. The first step will be discussed in sections 4.1 and 4.2.

4.1 Properties of signals in the muon planes

Not only muons can generate signals in the muon planes. Also γ-rays and neutrons can cause scintillation light and give rise to background. To be able to eliminate these spurious signals a coincidence between 2 or more muon planes is required. A hardware trigger is set to identify signals from the muon board where 2 planes are triggered in coincidence and both have a signal larger than 30 mV, these are then kept. When NEMENIX sees a signal, the hardware trigger also fires and the output of the muon planes is stored as well. Afterwards a software trigger of 6 mV is applied to these data, this trigger is referred to as trigger 0. Therefore all the events where the muon board triggered itself and only some events where NEMENIX triggered the muon system are kept.

These signal waveforms are stored in root files which each contain data acquired during approximately 30 minutes. Both data from reactor-on and -off periods are stored. To

access the information stored in the root files a program needs to be written. The C++ code used in this thesis is adapted from code provided by P. Van Mulders from the VUB. The code reads all the events stored in a given root file and skips over events used as calibration which are recognized by the software trigger -1. The first event that doesn't have a trigger value of -1, is used to determine the CPU start time of the run. The last event of the data file is used as the CPU stop time. The difference between these 2 values then gives the exact value of the run duration.

A first step is to investigate events which have a signal in the muon board. As mentioned in the beginning of this section, the signals in the muon board are kept by software trigger 0 and are found in digitizer board 4. As can be found in table 3.3 the different muon planes correspond to different VME channels, labeled 0 to 3. The code runs over the different channels of board 4 when a software trigger 0 event is detected and stores the waveform of all 4 channels. As mentioned in section 3.1 the PMTs give a negative pulse as an output. However to proceed one wants to work with positive signals and so the signal is inverted to obtain the positive peaks pictured in the following figures. Before the inversion, the pedestal is subtracted form the signal. This is the dark current from the PMT.

All stored events have either at least 2 channels with a peak over 30 mV, or signals above 6 mV, as mentioned in the first paragraph of this section, but this does not necessarily mean that all events contain a real muon signal. One could for example have an event where NEMENIX triggered the muon boards and where a signal above 6 mV, but not much larger, is detected in one of the channels. This is not likely to be a muon as there is no coincidence measured between the muon planes and a muon should also give a much higher peak as they are very energetic. It is more likely that the signal is coming from a particle, for example a gamma or a thermalized neutron, escaping from NEMENIX itself and passing one of the detectors on its way out. An example of such an event is shown in figure 4.1 where the waveforms of the signals in the 4 muon channels are displayed. On the x axis the sample number is displayed which is an indication of time. A unit of sample number corresponds to about 10 ns. On the y axis the amplitude of the signal is expressed in ADC counts. As shown in section 3.4 1 ADC count corresponds to 0.14 mV. The software threshold of 6 mV thus corresponds to about 43 ADC counts.

It is also possible that a muon passes NEMENIX and only 1 muon plane due to geometrical effects. In this case NEMENIX will trigger the muon boards and the software trigger will also keep the signal as it is large enough to pass the threshold. In this case a large peak will be seen in only 1 muon channel of board 4. Of course one can not know for sure whether this kind of signal is due to a muon. A more conclusive answer can be found by combining the signal from the muon board to that of NEMENIX. When one can follow the path of the particle through the NEMENIX detector and one sees it for example leaving at a side where no other muon plane is situated, it is to be expected that

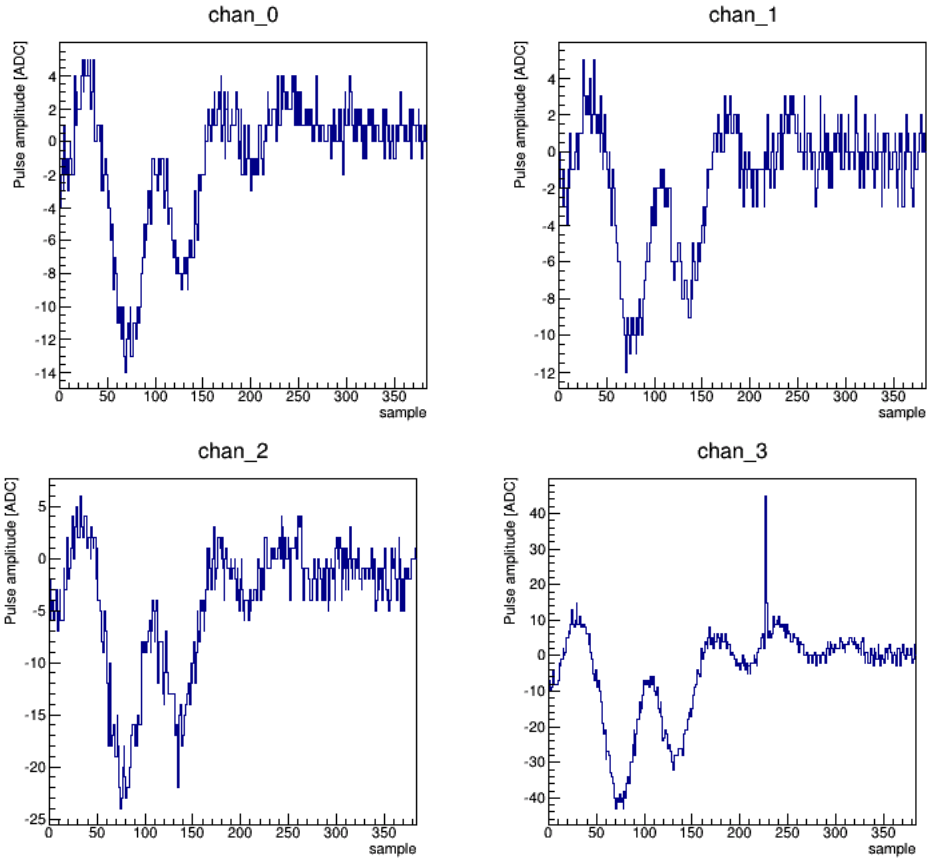

Figure 4.1: Spurious muon signal out of data file NEMENIX_long_24Mar2014_11h14.dat.root.

only 1 plane gives a signal. At the same time one excludes the possibility of an energetic particle escaping NEMENIX and giving a signal in one of the muon boards as this would give a signal originating somewhere in NEMENIX and not passing straight through. An example of a single peak can be found in figure 4.2, where only in channel 3 a large peak is observed. Until matching with NEMENIX is performed it is not possibly to conclusively state this event to be a muon signal.

By investigating different data files, it became clear that there are no peaks to be seen in channel 1. This means that no signals are detected in the small, right vertical muon plane. This could be due to an incident during the installation of the muon planes at BR2. For example, the PMT could be broken or the readout cable could be disconnected. In any case, nothing but noise is detected, so there are also no coincidences to be seen with channel 1.

Another general characteristic of the waveforms in the muon channels is the form of the noise. As can be seen in the figures 4.1 and 4.2, but also more explicitly in figure 4.3, the noise has the same shape in all the channels. This points to some kind of electronic noise

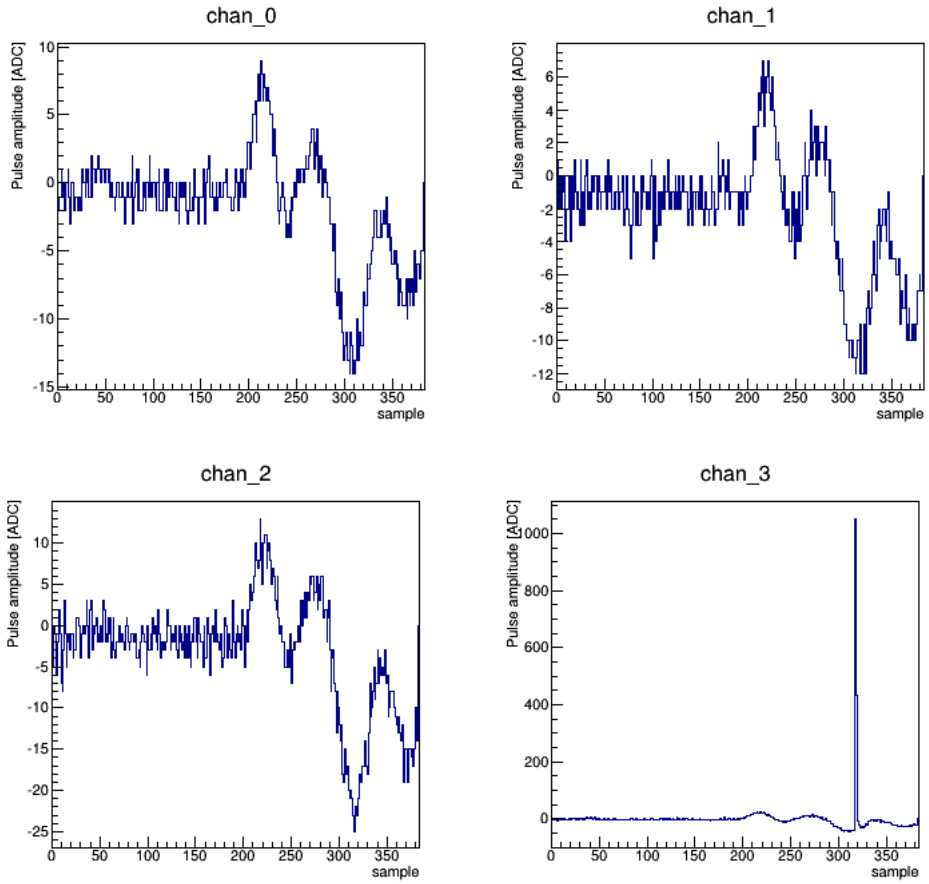

Figure 4.2: Single muon signal out of data file NEMENIX_long_24Mar2014_11h14.dat.root.

which is picked up and this can also be seen in NEMENIX signals [38]. It is also apparent that the waveforms in channel 3, the upper large detector, have in general a larger amplitude. This could be explained by a more sensitive PMT. Although the same type was used for each muon plane, all individual PMTs can differ slightly from each other. The effect could also be caused by the cabling.

It is useful to look at the maximum amplitude in each channel for every event, shown in the figures 4.4, 4.5 and 4.6. For these plots, for a certain event, all channels with a maximum amplitude higher than 40 ADC counts are taken into account, which explains the empty bins in the region below this value. No plot is made for channel 1 as this gives no useful signals anyway.

It can be seen that in figure 4.4 the largest bin is situated just above the threshold value of 40 ADC counts. This is to be understood as a lot of events in channel 0 being noise instead of muon signals. This is normal as channel 0 corresponds to the small, left vertical plane. The chance of a muon passing is smallest for the vertical planes. Thus, when an event is kept by software trigger 0, the peaks are most likely to be seen in the large muon

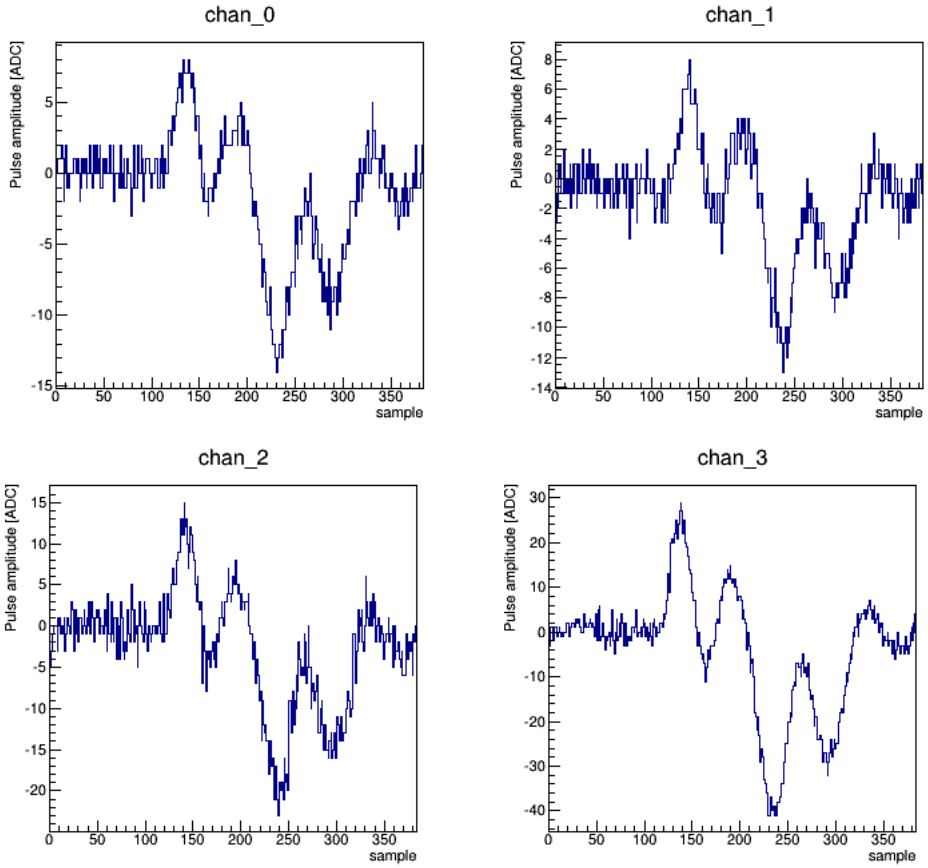

Figure 4.3: Noise in the muon channels out of data file NEMENIX_long_24Mar2014_11h14.dat.root.

panels corresponding to channel 2 and 3.

This difference can be seen when comparing figure 4.4 to 4.5, where the last one has the distribution peak located around 165±15 ADC counts. Obviously here, the real muon signals contribute more as the chance of finding peaks in the large detectors, channel 2 and 3, is greater than for small detectors. Also a much longer tail can be seen which points to the presence of energetic muons.

In channel 3, see figure 4.6, the peak is located even higher at a value of 315±15 ADC counts. The distribution should in principle be the same as that in figure 4.5, but as mentioned before channel 3 in general shows a larger amplitude, this explains the shift to the right. The peak for channel 3 is therefore also wider than the peak for channel 2. The full width at half maximum (FWHM) is measured by fitting a gaussian curve to the peaks in figures 4.5 and 4.6. This results in a FWHM of 146±1.9 ADC counts and 318±4.8 ADC counts, respectively for channels 2 and 3. Out of these results it is clear that the gain of channel 3 is 1.9±0.3 (315/165) times as high as that of channel 2 as the ratios between

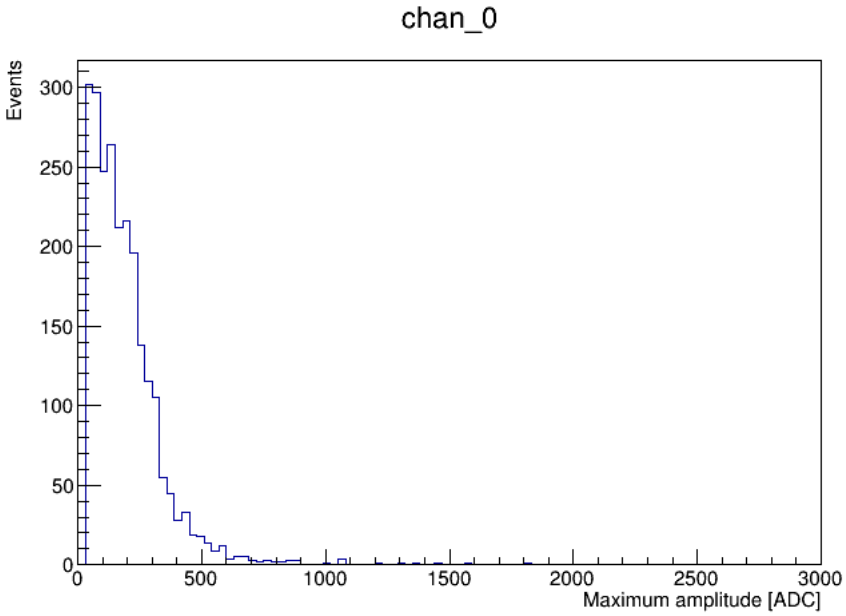

Figure 4.4: Maximum amplitude distribution for channel 0.

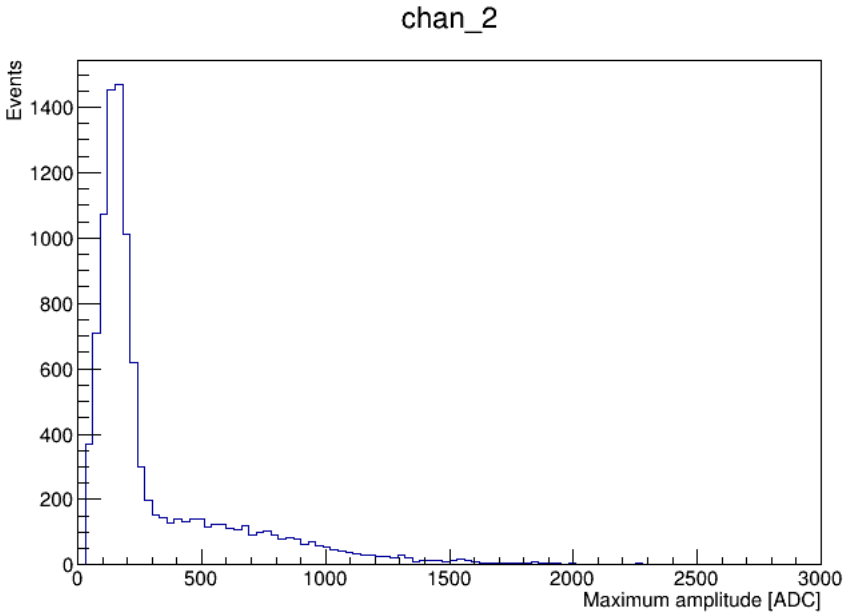

Figure 4.5: Maximum amplitude distribution for channel 2.

the ADC counts and the FWHM are compatible within errors for channels 2 (1.13±0.11) and 3 (0.99± 0.06). The difference in gain is probably a combination of a more sensitive PMT and a better optical coupling between scintillator, wavelength shifter and PMT.

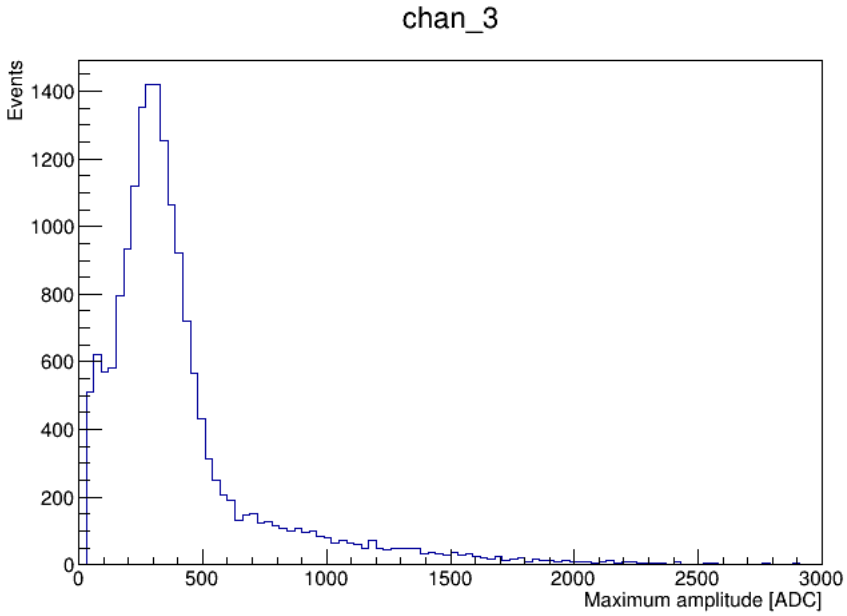

Figure 4.6: Maximum amplitude distribution for channel 3.

4.2 Properties of coincidences in the muon planes

Without matching with the NEMENIX signals a muon event can be identified by looking for coincidences between different muon channels. Therefore the waveform of the signal in a certain channel is scanned for peaks which exceed a certain threshold value and these waveforms are then stored. For a certain event, this is done for the 4 channels and one can then look for coincidences. This is done by looking for peaks in different channels that occur in a narrow time window from each other. As already mentioned in this section, sample number is used as a time unit and therefore the time window is expressed as a sample difference between peaks. The sample difference for a certain peak is chosen as the middle of the peak. An example of a coincidence can be found in figure 4.7. A coincidence is found between the first peak in channel 2 and the single peak in channel 3. In this case a muon passed the upper and the lower large muon planes.

As will be discussed in section 4.3, it is also possible for a muon to pass through 3 muon planes. As channel 1 is dead, only coincidences between channel 0, 2 and 3 can be seen in this category. An example is displayed in figure 4.8. Here a muon passes at a time corresponding to a sample number a bit below 50.

The number of coincidences is of course dependent on the values of the threshold and the sample difference between peaks that are considered as being due to the same muon. The threshold parameter is very important in the selection of signals. As could be seen in section 3.3 the number of single counts and the efficiency in figures 3.6 and 3.7 drops down quite rapidly when one passes a certain threshold. On the other hand, the number

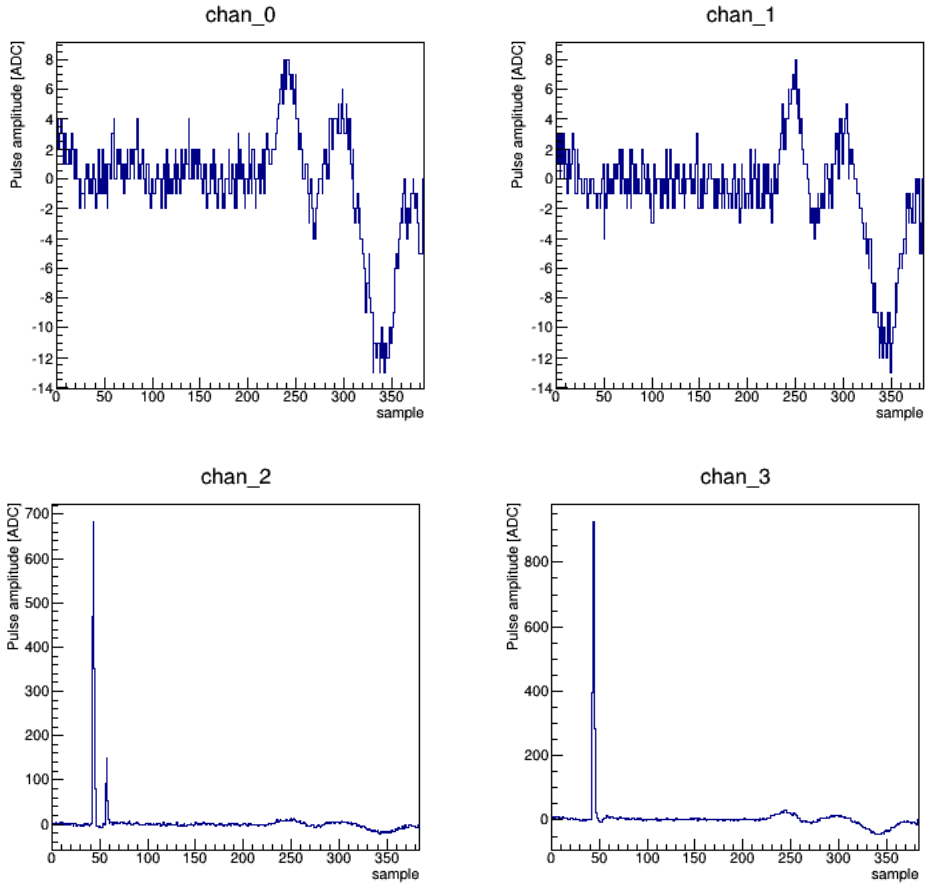

Figure 4.7: Muon coincidence between 2 channels out of data file NEMENIX_long_23Mar2014_15h43.dat.root.

of signals would go up steeply if one was to lower the threshold even more than was done in the previous mentioned figures. One would then count a lot of background signals as being muons. Obviously, this needs to be avoided. By investigating the signals of the muon planes on an oscilloscope it became clear that an average muon signal has a maximum amplitude of about 200 mV. As was determined during the efficiency measurements, a threshold of 30 mV is appropriate for the muon panels at hand. Therefore the hardware trigger for muon panels triggering themselves is also set at this value, see the beginning of this section.

As can be seen in figure 4.9, the slope of the number of peaks in channel 2 during a 30 minutes measurement, data file NEMENIX_long_23Mar2014_15h43.dat.root, gets a lot steeper below a certain threshold value where one starts to pick up a lot of noise. This is around 100 ADC counts which corresponds to about 15 mV. This value matches the average size of noise, determined by looking at the signals of the muon panels with the help of an oscilloscope. The same trend in seen in the other channels.

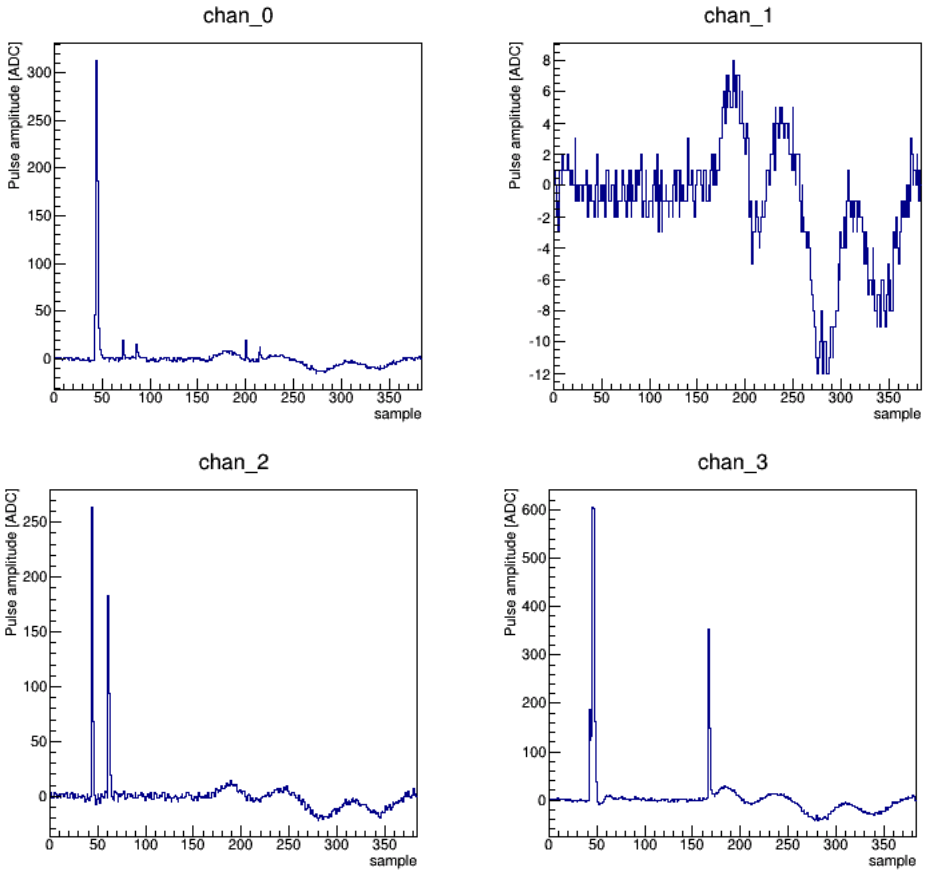

Figure 4.8: Muon coincidence between 3 channels out of data file NEMENIX_long_23Mar2014_15h43.dat.root.

Contrary to figure 4.9, one can not see a change in slope in figure 4.10 where the number of coincidences from the same measurement is shown in function of threshold. These data points are obtained by setting the sample difference to a value of 10. Because there is no change in slope for the coincidences one can conclude that one is still able to distinguish true coincidences and that noise does not contribute very much to the number of coincidences. In any case not as much as it does for the number of peaks in each individual channel.

The second important factor in the determination of the number of coincidences per data file is the sample difference. When choosing this too large one will match signals which are not in true coincidence but rather accidentally happen to be close to each other in time. On the other hand, when one chooses this value too small, true coincidences can be missed as the shape of the signal of a passing muon is not necessarily the same in all the channels through which it passes. Therefore the sample values of the 2 corresponding peaks, which are determined as the middle of the peak, can be shifted enough so that they are not seen as a coincidence. In figure 4.11 the distribution of the number of coincidences

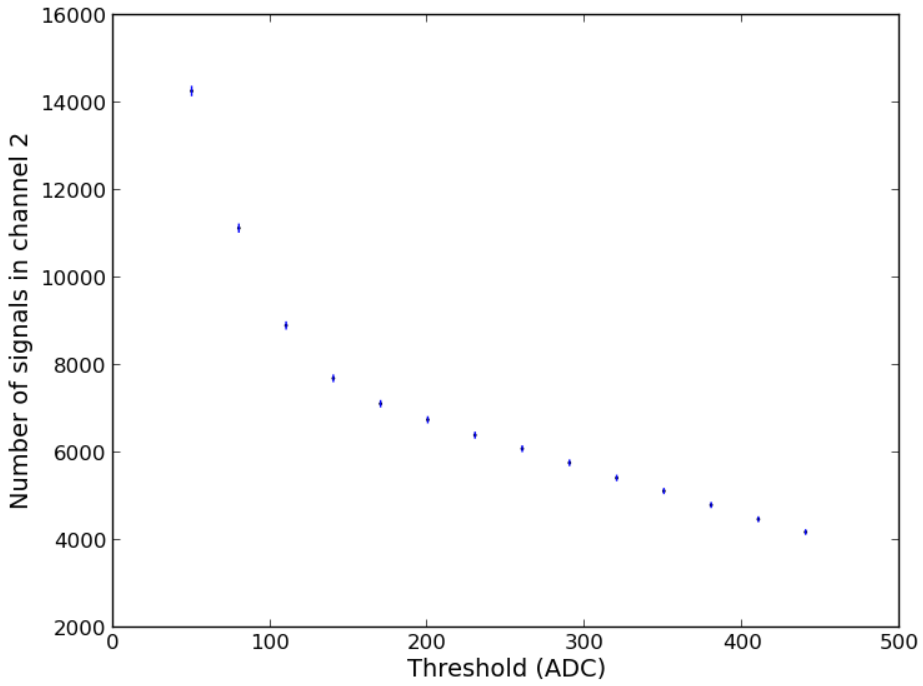

Figure 4.9: Peaks in channel 2 in function of threshold.

in function of sample difference can be seen for a threshold of 100 ADC counts. As can be seen most coincidences occur for a sample difference equal to 2 and the distribution drops down very rapidly after the value of 5. Small peaks can be seen after this value however. When one plots the same distribution for a threshold of 200 ADC counts, see figure 4.12, these peaks disappear indicating that these were just spurious coincidences. To include all real coincidences it is thus safe to chose a value of 10 for the sample difference.

All figures in this section are made with file NEMENIX_long_23Mar2014_15h43.dat.root which consists out of 250207 events and covers a run duration of almost 30 minutes. The reactor was not running on the 23rd of March. In principle all the previous mentioned properties of muon signals should not be affected by the activation of the reactor. All of the discussed muon signal properties are revisited with the data file NEMENIX_long_30Mar2014_15h08.dat.root which consists out of 206515 events and also covers a 30 minutes run. On the 30th of March the reactor was turned on. No differences between reactor-off and -on periods are found, as expected.

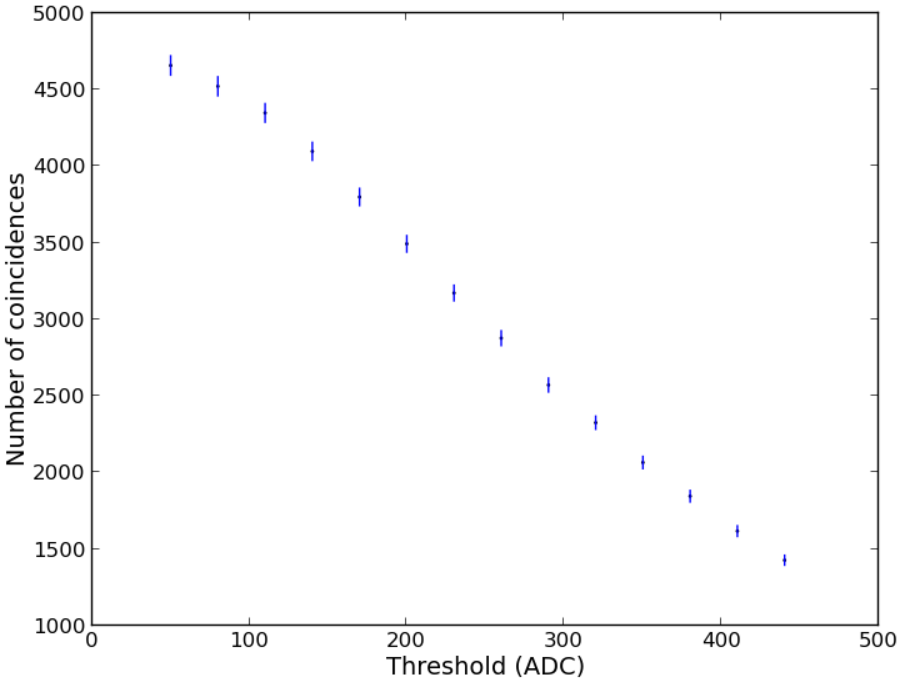

Figure 4.10: Coincidences in function of threshold, for a sample difference of 10.

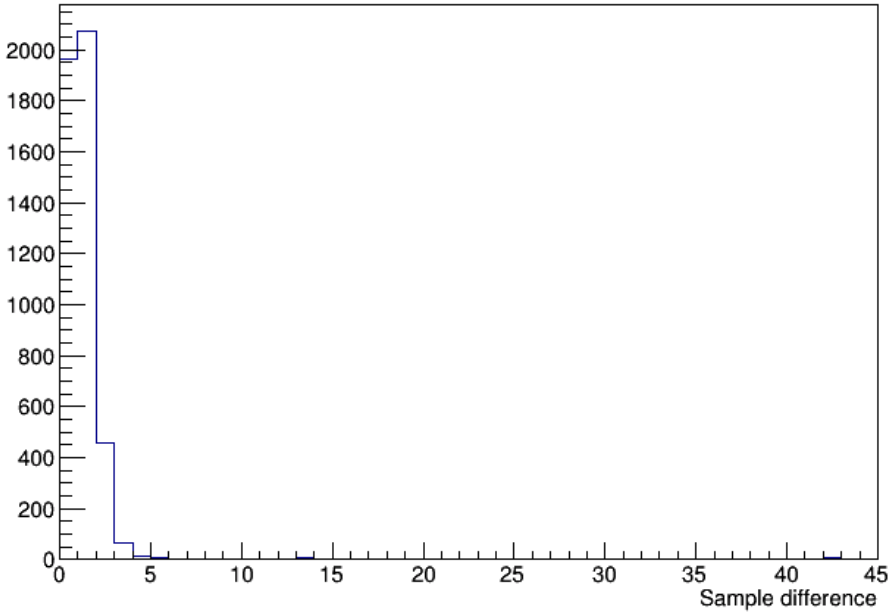

Figure 4.11: Coincidences in function of sample difference, for a threshold of 100 ADC counts.

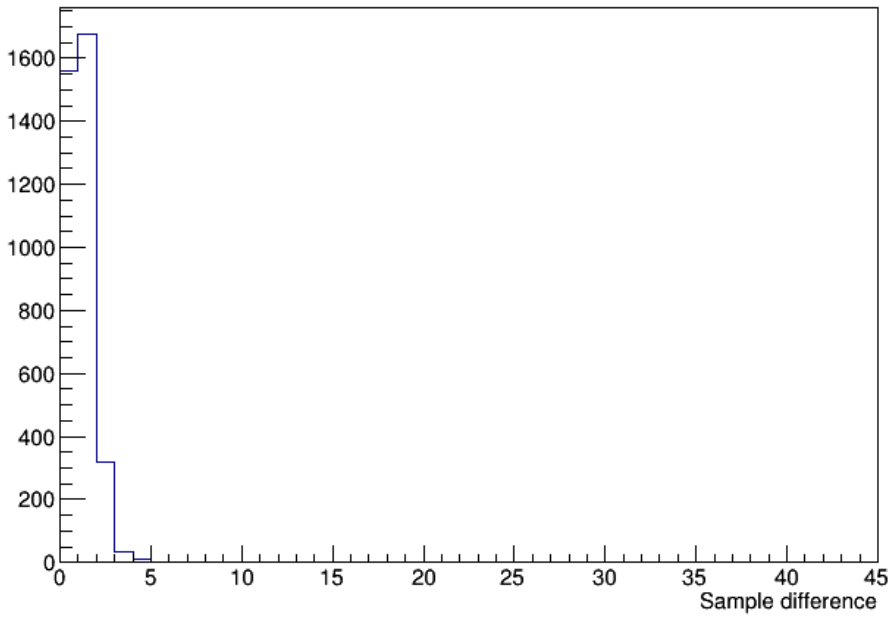

Figure 4.12: Coincidences in function of sample difference, for a threshold of 200 ADC counts.

4.3 Geometric efficiency at BR2

When one wants to measure the rates of muons at BR2 and compare these to the rates measured at Ghent, one needs to take the different geometrical efficiency into account. The detectors at the BR2 site are much more separated than in the Ghent efficiency setup so that muons can easily cross only 1 detector without passing through one of the other muon planes. As discussed in section 4.2 a muon is identified by requiring a coincidence between at least 2 of the muon planes as long as the matching of signals with the NEMENIX detector remains impossible. Therefore a lot of muons passing the detector system will not be identified as they only hit one of the muon planes and this will have a large influence on the measured rate of muons, see section 4.5.

As is done for the determination of the geometric efficiency in section 3.3 a C++ Monte-Carlo simulation is written. In the same way as for the other C++ simulation, a muon is generated at a random position with a random direction. The track of the particle is reconstructed and for every muon panel, as well as for the NEMENIX prototype, it is checked whether the track intersects the detector. The geometry that is used in the simulation is shown in figures 4.13 and 4.14, where respectively the front and the top view of the detector system are displayed. Some of the dimensions are educated guesses as the setup at BR2 was not measured in detail.

As long as there is no matching between the muon planes and NEMENIX signals, muons are only identified as coincidences between different muon planes. Therefore the rate of

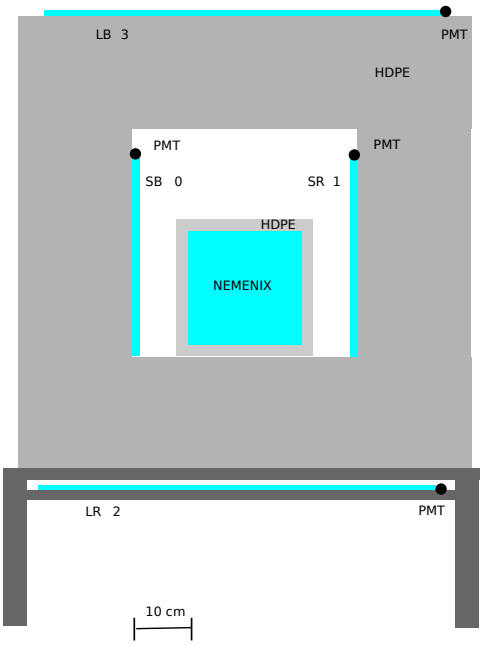

Figure 4.13: Sketch of the setup at BR2, front view.

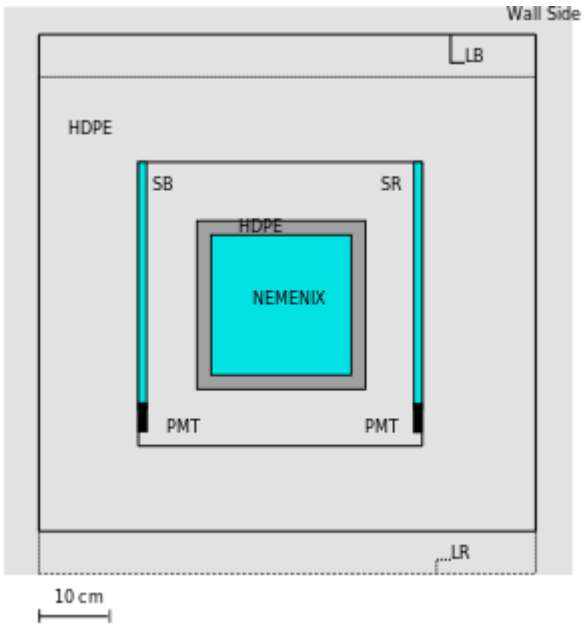

Figure 4.14: Sketch of the setup at BR2, top view.

muons will depend on the geometrical probability that a passing muon will hit 2 or more muon detectors. To determine this factor the ratio of the number of coincidences between any 2 muon planes and the number of tracks that hit at least 1 muon plane is calculated. In this way an efficiency of 46.2±1.7 % is obtained.

It is also found that only 0.70±0.03 % of all events pass through the NEMENIX detector without hitting any of the muon planes on their way. This is a very small fraction, so when matching of the signals of NEMENIX and the muon planes will be done, it will be very unlikely that a muon will need to be identified solely by its signal in the NEMENIX prototype. This means that the installation of the muon detectors will give a very efficient way of telling whether the signal in NEMENIX is due to a muon or not. Of course one still needs to take into account that due to the intrinsic efficiencies of the muon planes, it will still be possible for a muon to pass through a combination of muon planes and NEMENIX while only being detected by the latter.

Another effect which can be found with this simulation is the number of coincidences between muon planes which will not be seen by NEMENIX. This amounts to a total of 80.4±0.1 %. So it is expected that muon rates determined in section 4.5 will be higher than muon rates observed in the NEMENIX detector. If only geometrical arguments are used and one neglects efficiencies and shielding, the rate measured by NEMENIX should thus only be about 20 % of the rate observed with the muon detectors.

Coincidences can be seen between different channels, so it is useful to understand how these rates should compare to each other. As atmospheric muons have a $\cos^2\theta$ distribution, the chance of them impinging on the detector system from above is larger than for hits on the sides. The simulation makes it clear that very few muons should hit both vertical detectors and most of the coincidences should be seen between the upper and the lower detector. Due to symmetry reasons, the rate of coincidences between the left or right detector with one of the horizontal large detectors should be the same. However, as can be seen in table 4.1, there should be a difference in number of coincidences between the upper or lower detector with one of the small vertical ones. As can be seen in figure 4.13 the lower detector is somewhat closer to the small ones than the detector on the top of the HDPE shielding, which explains why there are more coincidences between the lower and side detectors. The difference is small and should anyway be treated with care as the dimensions used in the simulation are only estimates. Because of the expected influence on the rates of the position of the lower and upper detector with respect to the vertical ones, the dimensions are varied. A combination of 3 simulations was therefore used to obtain the results and errors mentioned in this paragraph. One of the simulation geometries is the one shown in figure 4.13, in the 2 others the lower and the upper detectors are respectively set 2 and 3 cm further away from the vertical ones.

As was already demonstrated in section 4.2 it is possible for a muon to pass through 3 muon detectors. The simulation shows that about 12.0±0.1 % of the coincidences go through 3 detectors. Of these events, 11±1 % also pass trough NEMENIX. It is also apparent that more than half of the coincidences with the small detectors are between 3 detectors instead of 2.

In table 4.1 the expected rates of coincidences between 2 specific channels to the total number of coincidences between 2 channels, obtained with the geometry simulation, are shown. To make it easier to compare with the next section, channel numbers are used instead of positions, see table 3.3 for the link between the 2.

Table 4.1: Fraction of coincidences, from the geometry simulation.

Combination of channels	Fraction of coincidences (%) (error)
0 & 2	4.07 (0.04)
1 & 2	4.08 (0.04)
0 & 3	3.64 (0.04)
1 & 3	3.63 (0.04)
2 & 3	84.01 (0.07)
0 & 1	0.57 (0.02)

To be able to compare the results of the simulation with the data, channel 1 is left out of the simulation. This gives the fraction of coincidences which are tabulated in table 4.2. Here the fractions are calculated with respect to the total number of coincidences, where triples are also included. For the coincidences between 2 channels a clear distinction is made between those which occur explicitly only in those 2 channels and those which can also be part of a triple coincidence, for example indicated as 0 & 2 & $\bar{3}$ and 0 & 2 respectively.

Table 4.2: Fraction of coincidences, from the geometry simulation where channel 1 is left out.

Combination of channels	Fraction of coincidences (%) (error)
0 & 2 & $\bar{3}$	4.14 (0.04)
0 & 2	11.10 (0.06)
0 & 3 & $\bar{2}$	3.69 (0.04)
0 & 3	10.66 (0.06)
2 & 3 & $\bar{0}$	85.21 (0.06)
2 & 3	92.18 (0.05)
0 & 2 & 3	6.96 (0.05)

The errors mentioned in tables 4.1 and 4.2 are binomial errors [1]. This is not entirely correct as one thus neglects the errors on the numerator and denominator, but it is a much better than the Poisson approach, where the standard deviation $\sigma = \sqrt{N}$. In the latter one would propagate the individual Poisson errors of the numerator and denominator, but as these errors are correlated a very conservative error would be obtained. A better approach is thus to use a binomial error.

4.4 Comparison of muon rates with simulation

It is useful to have a look at how the coincidences in the data are divided over the different muon planes. It is expected that most coincidences are seen between the upper (channel 3) and the lower large (channel 2) detectors as most muons are impinging the detector system straight from above due to their angular distribution, see section 4.3. In the same section it is also determined that it is slightly more likely for a muon to pass through one of the small detectors and the lower detector than through one of the small ones and the upper detector. These effects are confirmed in table 4.3 which contains data from the file NEMENIX_long_23Mar2014_15h43.dat.root. Coincidences with channel 1 do not exist as this channel is broken. The values in the table are for a sample difference of 10, which is an appropriate value as was discussed in the section 4.2. The threshold (T) is set at 200 ADC counts, around 30 mV, to eliminate all spurious coincidences. The same results are shown for a threshold of 300 ADC counts. For the coincidences between 2 channels again the distinction is made between those which occur only in those 2 channels and those which can also be part of a triple coincidence. The fractions are calculated with respect to the total number of coincidences, triples included.

The errors on the coincidences and peaks in table 4.3 are calculated following the Poisson distribution. However this is a conservative approach and is not the best suited one to use in this context [39]. This is due to the large probability of a muon passing a detector and also being detected, as can be seen in section 3.3 where the detector efficiencies are mentioned. Better would be to use binomial errors. Unfortunately this technique can not be applied here as some parameters are missing. For the binomial approach one has to know the exact number of trials, so the number of passing muons, and the exact probability that this muon will be detected. The number of trials can never be obtained in this kind of experiment. The efficiency measured in section 3.3 can not be used as the probability as this efficiency depends on certain parameters such as thresholds which are different at the BR2 reactor and in the Ghent setup. Therefore, Poisson errors, although conservative, are the most logical ones to use. For the fraction of coincidences the situation changes.

[1] For the binomial approach one has to know the exact number of trials N, in this case the number of coincidences between certain channels, and the probability of success p, this is the fraction of coincidences between certain channels. The standard deviation is given by $\sigma = \sqrt{N \times p \times (1-p)}$

Here, one knows exactly what the number of trials N is, namely the total number of coincidences, and the probability p is just the fraction itself. A binomial error calculation is thus possible. The downside of this approach is that one does not take into account the individual errors on the numerator and denominator. However, this approach is preferable to the conservative Poisson calculation where one would propagate the correlated Poisson errors.

In the third part of the table 4.3 it can again be noted that for the lower threshold channel 3 has more counts than channel 2, although they have the same detector size. This can be explained by the, in general, higher amplitudes seen in the former channel, as was mentioned in section 4.1, and thus counting of more noise and low amplitude signals in channel 3. The effect of this noise disappears when the threshold is raised to 300 ADC counts. This shows that a threshold of 300 ADC counts, about 42 mV, is a more appropriate value for channel 2 and 3.

The middle part of table 4.3 could be compared with table 4.2. However this discussion would only take into account the geometrical effects at BR2. It makes more sense to include the detector efficiencies. However, it must be noted that the efficiencies measured in section 3.3 are only valid in the Ghent setup, where geometry and thresholds differ from those used in the BR2 setup. It is thus an approximation to use these in combination with the geometrical effects at BR2 to get an estimate of the expected fractions of coincidences.

As summarized in table 3.2 all working detectors in the system have a different intrinsic efficiency. To know which ratio of coincidences, $N_{a\&b}/N$ to expect in a certain channel combination a&b, where N is the total number of expected coincidences, one must take into account the amount of these coincidences which are missed due to the efficiency of a and b. Another aspect is the number of events which pass through 3 detectors, a, b and c, but only give a signal in detectors a and b due to the efficiency of detector c. One thus gets the following equations to obtain the expected ratios, where the $G_{a\&b}$ is the number of geometrical expected coincidences:

$$\begin{aligned}
N_{0\&2\&\bar{3}} &= 0.858 \times 0.841(G_{0\&2} + (1-0.799)G_{0\&2\&3}) \\
N_{0\&3\&\bar{2}} &= 0.858 \times 0.799(G_{0\&3} + (1-0.841)G_{0\&2\&3}) \\
N_{2\&3\&\bar{0}} &= 0.841 \times 0.799(G_{2\&3} + (1-0.858)G_{0\&2\&3}) \\
N_{0\&2\&3} &= 0.841 \times 0.799 \times 0.858(G_{0\&2\&3}) \\
N_{0\&2} &= N_{0\&2\&\bar{3}} + N_{0\&2\&3} \\
N_{0\&3} &= N_{0\&3\&\bar{2}} + N_{0\&2\&3} \\
N_{2\&3} &= N_{2\&3\&\bar{0}} + N_{0\&2\&3} \\
N &= N_{0\&2\&\bar{3}} + N_{0\&3\&\bar{2}} + N_{2\&3\&\bar{0}} + N_{0\&2\&3}
\end{aligned} \tag{4.1}$$

Table 4.3: The number and fraction of coincidences for each combination of channels, for a sample difference of 10, and the number of peaks in each channel.

Combination of channels	Coincidences for T=200 ADC counts (error)	Coincidences for T=300 ADC (error)
0 & 2 & $\bar{3}$	219 (14.8)	85 (9.3)
0 & 2	278 (22.5)	113 (14.6)
0 & 3 & $\bar{2}$	59 (7.7)	23 (4.8)
0 & 3	118 (15.4)	51 (10.1)
2 & 3 & $\bar{0}$	3155 (56.2)	2357 (48.6)
2 & 3	3214 (63.9)	2385 (53.9)
Combination of channels	Fraction of coincidences for T=200 ADC counts (%) (error)	Fraction of coincidences for T=300 ADC (%) (error)
0 & 2 & $\bar{3}$	6.3 (0.5)	3.4 (0.4)
0 & 2	8.0 (0.5)	4.5 (0.5)
0 & 3 & $\bar{2}$	1.7 (0.3)	0.9 (0.2)
0 & 3	3.4 (0.4)	2.1 (0.3)
2 & 3 & $\bar{0}$	90.4 (0.5)	94.5 (0.5)
2 & 3	92.0 (0.5)	95.7 (0.5)
0 & 2 & 3	1.7 (0.3)	1.1 (0.3)
Channel	Peaks above T=200 ADC counts (error)	Peaks above T=300 ADC counts (error)
0	750 (50.4)	281(16.8)
2	6747 (134.3)	5651 (75.2)
3	8475 (143.7)	5469 (74.0)

Table 4.4: Fraction of coincidences expected from geometry and detector efficiency.

Combination of channels	Expected fraction of coincidences (%) (error)
$N_{0\&2\&\bar{3}}/N$	4.94 (0.05)
$N_{0\&2}/N$	9.97 (0.06)
$N_{0\&3\&\bar{2}}/N$	4.09 (0.04)
$N_{0\&3}/N$	9.12 (0.06)
$N_{2\&3\&\bar{0}}/N$	85.94 (0.07)
$N_{2\&3}/N$	90.97 (0.06)
$N_{0\&2\&3}/N$	5.03 (0.05)

The results obtained by combining the equations 4.1 with the geometry simulation are shown in table 4.4. These can now be compared with the data, more specifically to the

middle part of table 4.3. It can be seen that the data do not correspond to the combination of the simulation and efficiencies very well. None of the fractions match within errors. A large part of the error probably lies in the threshold settings. The efficiencies of the detectors were measured for certain values of threshold, as can be seen in section 3.3. It was determined that the large detectors have a good efficiency at a threshold of about 45 mV, while the small detectors detect best around a threshold of 30 mV. It can be seen in figures 3.6 and 3.7 that the efficiency of the small detectors starts to drop down around a threshold of 40 mV.

Looking at the fractions obtained for a threshold of 300 ADC counts, 42 mV, it can be reasoned that most of the inconsistencies with the simulation come from channel 0. This can be seen most clearly in the fractions of $2\&3\&\bar{0}$ and 2&3. Here the difference between data and simulation is much larger when channel 0 is explicitly excluded form the coincidence between channel 2 and 3 than when it is not. If channel 0 would trigger at a higher rate, 2&3 would be higher and this would then be more consistent with the simulation. More triggering in channel 0 should also increase the triple coincidences. The lower trigger rate of channel 0 can be explained by the threshold setting, which in this case causes the efficiency of channel 0 to drop down. For the threshold of 300 ADC counts it can also be concluded that channel 2 is matching the simulation values best. This can be seen as the values $0\&3\&\bar{2}$ and 0&3 differ about a factor 2, which is also the case for these values obtained from simulations.

The fractions obtained for a threshold of 200 ADC counts, 28 mV, are also not compatible with the simulation results in table 4.4. In this case, it is not channel 0, but channels 2 and 3 which cause the discrepancies. For the large detectors this threshold setting allows for a lot of noise and it should thus be avoided. It is much more difficult to see the exact influence of these effects as the coincidences within channel 2 and 3 contribute immensely to the total number of coincidences and therefore to the denominator which is used to calculate all the other fractions as well. It is thus not straightforward to discriminate the influence of numerator and denominator in this case.

It would be very useful to be able to set a different threshold for each channel. This would help to eliminate the difference in efficiencies and would clarify which discrepancies between data and simulation still exist. Unfortunately this was not possible within the time frame of this thesis.

The large difference between fractions 0&2 and 0&3, or between fractions $0\&2\&\bar{3}$ and $0\&3\&\bar{2}$, could also be explained by a threshold setting if it could be demonstrated that the efficiency of channel 3 reaches its peak value at a larger threshold than the value where channel 2 reaches its maximal efficiency and larger than the threshold of 300 ADC counts. In this case the fractions of 0&3 and $0\&3\&\bar{2}$ would go up and the difference with

simulations should be reduced.

Another possible cause for this latter discrepancy is the shielding at the BR2 site, which could change the angular distribution of muons impinging on the detector system. On the left and right side of the detector system lead walls of about 40 cm thick are positioned. A lead wall is quite effective in shielding atmospheric muons, 40 cm should already reduce the flux by 18 % [40]. Muons crossing the lead with a large zenith angle cross even more than 40 cm of material, thus reducing the flux even further. This does cause attenuation from muons and thus should lower the number of coincidences seen between channel 0 and 2, compared to those between channel 0 and 3, as the former coincidences are generally caused by muons with a larger incident angle. This however contradicts the effect seen in the data and could only provide a solution if something did go wrong with the cabling and channels 2 and 3 are switched. Extra measurements at BR2 could confirm or disprove this.

4.5 Muon rates at BR2

A last check whether the muon system is capable of identifying passing muons and differentiating from other backgrounds can be found by looking at the rate of muons over a large time period. In figure 4.15 one can see the rate of muon coincidences on the basis of a threshold set at 200 ADC counts and a sample difference of 10. This plot was made with results generated by N. Ryder, who was able to run the data analysis code over a large data sample. It can be noted that the rate is very stable over reactor-on and -off periods. The reactor-off period on this plot is from the 25th of March to the 15th of April. This is what is expected when one measures only muons as this rate does not depend on the status of the reactor. Other backgrounds such as γ-rays and neutrons should go up during reactor-on periods, so it is clear that the measured coincidences are due to muons only. The rate of coincidences has a value of 2.67 ± 0.07 Hz.

A very crude comparison can be made with the rates obtained in Ghent. Of course these can not be compared in a correct way as the geometries, shielding effects and efficiencies are different in the Ghent and BR2 set ups. However, it could be important to understand if and why there is a difference. The comparison is made with the rate of coincidences between the upper and lower detector in the Ghent efficiency setup discussed in section 3.3. Here one looks at the muons going through the surface of a small detector and with a very large probability that a muon which passes the upper detector also passes the lower detector. A rate of 14.0 ± 0.2 Hz is seen. However, when one wants to compare this to the rate of BR2 where most of the coincidences are seen between the 2 large detectors, this rate should be corrected with a factor 4, which is the difference in area between a small and large detector. One thus obtains a rate of 56.0 ± 0.8 Hz. A large discrepancy is thus observed between the rates at Ghent and at BR2. This can be mediated somewhat by

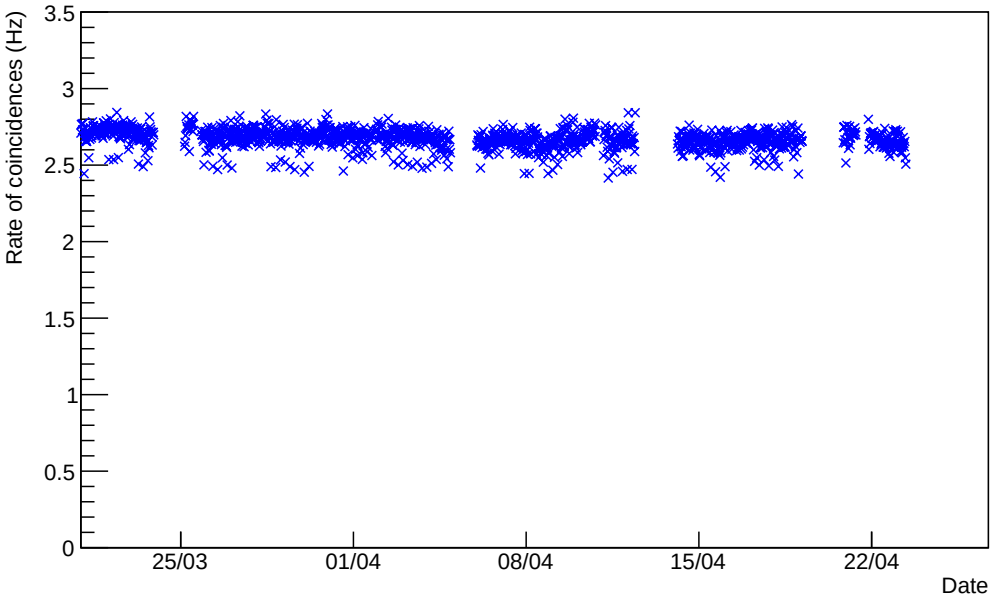

Figure 4.15: Muon coincidence rate, for a threshold of 200 ADC counts and a sample difference of 10.

taking into account that the geometrical efficiency is much lower at BR2. Monte Carlo simulations, see section 4.3, show that only 46.2 % of muons actually give a coincidence. This still leaves about 25.9±0.4 Hz as the expected rate, given the input from the Ghent measurement. Part of this inconsistency could perhaps be explained by the shielding at BR2, but not all materials and their thicknesses are known so that this effect can not be quantified. Although one can make an estimated guess by stating that muons coming from behind the reactor will not reach the detector system due to the very heavy shielding present around the reactor structure. Only measurements of the muon rates with the help of the Ghent electronics, discussed in section 3.2, at the BR2 site can give more clues towards solving this problem.

Chapter 5

Conclusions and outlook

The SoLid experiment is designed to prove or set upper limits on the existence of a sterile neutrino. It therefore tackles the problem of the reactor antineutrino anomaly.

In the summer of 2014 the SoLid detector will be built and it will take data starting from November. To evaluate possible construction and data-taking problems, the NEMENIX prototype was built. Collecting data with this prototype will also help to evaluate backgrounds which are present at the BR2 reactor. Among these are the atmospheric muons which are so energetic that they will normally pass straight through the detector.

As the NEMENIX prototype is quite small, 4 extra muon detectors, 2 small and 2 large ones, are installed to make the identification of muons easier. The first part of this research was to characterize the muon panels. As shown in section 3.3 the efficiencies of the detectors were determined in function of threshold for the small ones and in function of HV power for the large ones. The efficiencies of the small detectors were corrected for the geometrical effects of the setup. In this way efficiencies of 91.6±1.2 % (SR), 85.8±1.7 % (SB), 84.1±1.0 % (LR) and 79.9±0.9 % (LB) were determined. A high voltage setting of 1.4 kV proved to be adequate for the 4 detectors. The appropriate thresholds were found to be 30 mV for the small detectors and 45 and 50 mV for LR and LB respectively. After the characterization of the muon detectors, these could be installed at the BR2 reactor.

The second part of this thesis includes the analysis of muon signals in the muon panels. First individual signals were investigated in section 4.1. It was discussed that on the basis of single signals it is difficult to conclude the passing of a muon. The signal could also be due to some particle escaping from NEMENIX or due to a γ-ray or neutron. Therefore it is better to identify muons through the detection of coincidences of signals. It was noted that the right small detector, channel 1, does not give any signals and therefore it is concluded that this detector must have been damaged during installation at the BR2 reactor. It was also shown that the LB detector, channel 3, has a gain 1.9±0.3 times as high as that of the LR detector, channel 2.

Investigating the muon coincidences in section 4.2 showed that a value of 10 for the sample difference, about 100 ns, is well suited to detect almost all real coincidences and discriminate against accidentals. Combining the geometrical effects at the BR2 reactor, section 4.3, with the efficiencies determined in Ghent, section 3.3, one can obtain the fraction of expected coincidences between different channels. These values can then be compared with the fractions present in the data. This was done in section 4.4 and it was seen that there are large discrepancies. The most likely explanation is the threshold setting which has the same value for all detectors. Due to this, the efficiencies of one or more muon detectors can be lower or higher than those measured in the Ghent setup. This could be solved by adjusting the data analysis code so that a threshold can be set for each channel separately, to the value determined in section 3.3.

Measuring the rate of coincidences, section 4.5, shows that a stable rate is obtained during reactor-on and -off periods. This shows that mostly muons are detected and there is no influence of γ-rays or neutrons which would give a higher rate during reactor-on cycles. The rate obtained over a large data taking period is 2.67 ± 0.07 Hz. Unfortunately this does not match the rate expected from the measurements at Ghent combined with the geometric effects present at the BR2 reactor. An explanation for this inconsistency could be found in the shielding at BR2 which could alter the angular spectrum of impinging muons. This effect could be measured by performing some tests at BR2 with the electronic circuit used in the efficiency measurements.

In this research the first steps towards the investigation of signals and coincidences from muons in the NEMENIX detector system were taken. It was not yet possible to combine the signals from the muon detectors with those from NEMENIX. However, this would be very interesting as it would show the capability of NEMENIX to detect muons and it would make the characterization of muons in the prototype detector much easier. These results would be necessary to determine whether or not extra muon detectors will be needed with the full SoLid detector.

Bibliography

[1] Povh, Rith, Scholz and Zetsche, *Particles and nuclei*. Springer, 6 ed., 2008.

[2] J. Beringer et al., "Review of Particle Physics," *Phys. Rev. D*, vol. 86, p. 010001, 2012.

[3] NEMO Collabortion, "Physics goals - Neutrinos," *http://nemo.in2p3.fr/physics/neutrinos.php*, 2004.

[4] S. M. Bilenky, "Neutrino. History of a unique particle," *arXiv:1210.3065*, 2012.

[5] F. Reines et al., "Detection of the free antineutrino," *Phys. Rev.*, vol. 117, p. 159, 1960.

[6] L. M. Lederman, "Observations in particle physics from two neutrinos to the Standard Model," *Nobel lecture*, vol. 392, 1988.

[7] M. L. Perl, "The new particles produced in electron-positron annihilation," *SLAC-PUB-1652*, 1975.

[8] DONUT collaboration, "Observation of tau neutrino interactions," *Phys. Lett. B*, vol. 504, pp. 218–224, 2000.

[9] S. W. Herb et al., "Observation of a dimuon resonance at 9.5 GeV in 400 GeV proton-nucleus collisions," *Phys. Rev. Lett.*, vol. 39, no. 5, p. 252, 1977.

[10] F. Abe et al., "Observation of top quark production in $\bar{p}p$ collisions with the Collider Detector at Fermilab," *Phys. Rev. Lett.*, vol. 74, p. 2626, 1995.

[11] ALEPH Collaboration (D. DeCamp et al.), "Determination of the number of light neutrino species," *Phys. Lett. B*, vol. 231, no. 4, pp. 519–529, 1989.

[12] IceCube Collaboration, "All About Neutrinos," *https://icecube.wisc.edu/info/neutrinos*, 2014.

[13] R. Davis, Jr. and D. S. Harmer and K. C. Hoffman, "Search for neutrinos from the sun," *Phys. Rev. Lett.*, vol. 20, p. 1205, 1968.

[14] K. S. Hirata et al., "Observation of ^{8}B solar neutrinos in the Kamiokande-II detector," *Phys. Rev. Lett.*, vol. 63, no. 1, p. 16, 1989.

[15] G. Conforto et al., "A complete solution to neutrino mixing," *Astropart. Phys.*, vol. 5, pp. 147–158, 1996.

[16] B. Pontecorvo , "Neutrino Experiments and the Problem of Conservation of Leptonic Charge," *Sov. Phys. JETP*, vol. 26, pp. 984–988, 1968.

[17] S. Eidelman et al., "Particle Data Group - The Review of Particle Physics," *Phys. Lett. B*, vol. 592, p. chapter 13, revised 2005.

[18] A. Bettini, *Introduction to elementary particle physics.* Cambridge, 6 ed., 2008.

[19] A. Y. Smirnov, "Neutrino mass hierarchy and matter effects," *Proc. of Sci.*, 2013.

[20] Hewett, J.L. et al., "Fundamental physics at the intensity frontier," *FERMILAB-CONF-12-879-PPD*, 2012.

[21] D. V. Forero et al., "Global status of neutrino oscillation parameters after Neutrino-2012," *Phys. Rev. D*, vol. 86, p. 73012, 2012.

[22] The Super-Kamiokande Collaboration, Y. Fukuda et al, "Evidence for oscillation of atmospheric neutrinos," *Phys. Rev. Lett.*, vol. 81, pp. 1562–1567, 1998.

[23] R. N. Mohapatra, A.Y. Smirnov, "Neutrino mass and new physics," *Ann. Rev. Nucl. Part. Sci.*, vol. 56, pp. 569–628, 2006.

[24] C. Athanassopoulos et al. (LSND Collaboration), "Evidence for $\nu_\mu^- \to \nu_e^-$ oscillations from the LSND Experiment at the Los Alamos Meson Physics Facility," *Phys. Rev. Lett.*, vol. 77, p. 3082, 1996.

[25] A. A. Aguilar-Arevalo et al. (MiniBooNE Collaboration), "Event excess in the MiniBooNE search for $\bar{\nu}_\mu^- \to \bar{\nu}_e^-$ oscillations," *Phys. Rev. Lett.*, vol. 105, p. 181801, 2010.

[26] J. N. Abdurashitov et al., "The Russian-American gallium experiment (SAGE) Cr neutrino source measurement," *Phys. Rev. Lett.*, vol. 77, p. 4708, 1996.

[27] GALLEX Collaboration, "Final results of the ^{51}Cr neutrino source experiments in GALLEX," *Phys. Lett. B*, vol. 420, no. 1, pp. 114–126, 1998.

[28] C. Giunti, M. Laveder, "Short-baseline electron neutrino disappearance, tritium beta decay, and neutrinoless double-beta decay," *Phys. Rev. D*, vol. 82, p. 053005, 2010.

[29] T. Schwetz, "Neutrinomassenspektrum: normal oder invertiert, und wieviele Masseneigenzustände gibt es?," *Seminar DPG Tagung*, 25th March 2014.

[30] G. Mention et al., "The reactor antineutrino anomaly," *Phys. Rev. D*, vol. 83, p. 073006, 2011.

[31] K. N. Abazajian, "Light sterile neutrinos: A white paper," *arXiv:1204.5379*, 2012.

[32] F. Yermia et al., "Search for oscillation with a lithium-6 detector at SCK•CEN BR2 research reactor," *Seminar Conseil Scientifique IN2P3.*

[33] G. F. Knoll, *Radiation detection and measurement.* Wiley, 2000.

[34] Super-Kamiokande Collaboration, "Outline of Super-Kamiokande experiment," *http://www-sk.icrr.u-tokyo.ac.jp/sk/index-e.html*, 2007.

[35] CERN, "Cosmic rays: particles from outer space," *http://home.web.cern.ch/about/physics/cosmic-rays-particles-outer-space*, 2014.

[36] U.S. NIM Committee, "Standard NIM Instrumentation system," *http://www.osti.gov/scitech/biblio/7120327*, 1990.

[37] R. G. Michel, "Detectors in instrumentation," *Lecture notes Chemistry 5337, http://rgmlab.chem.uconn.edu/teaching/chem-337/.*

[38] N.Ryder and P. Van Mulders, "Private communication,"

[39] M. Paterno, "Calculating efficiencies and their uncertainties," *FNAL/CD/-CEPA/SLD paterno@fnal.gov*, 2003.

[40] E. Aguayo et al., "Cosmic ray interactions in shielding materials," *PNNL-20693*, 2011.

[41] A. Vacheret et al., "Search for oscillation with a lithium-6 detector at SCK•CEN BR2 research reactor," *Seminar APC-Paris*, 24th May 2013.